

CK-MPM: A Compact-Kernel Material Point Method

MICHAEL LIU, Carnegie Mellon University, USA
 XINLEI WANG, ZenusTech Inc., China
 MINCHEN LI, Carnegie Mellon University, USA

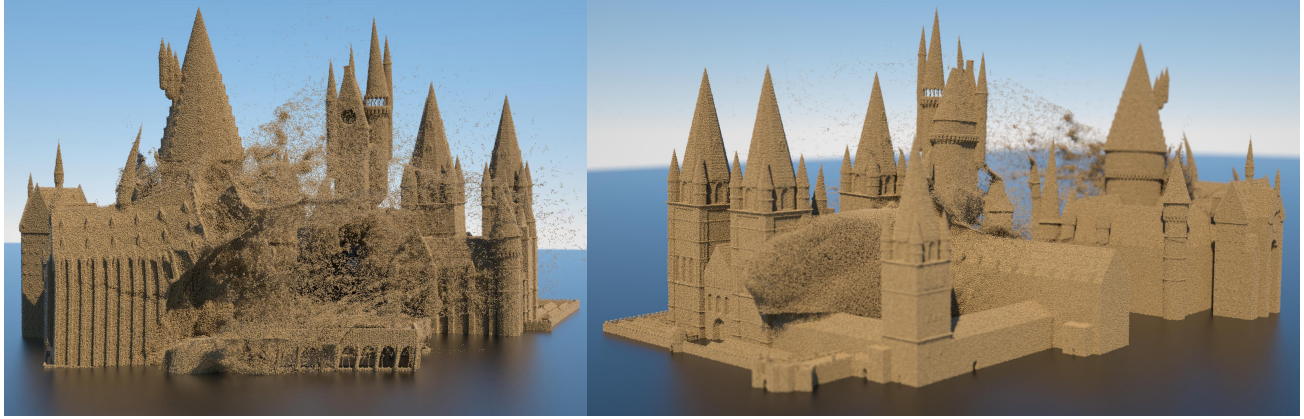


Fig. 1. **Sand Castle Crashing.** A large-scale simulation of a sandcastle’s destruction as a high-speed cannonball impacts it, performed using our compact-kernel material point method (CK-MPM). The sandcastle, modeled with 45.9 million particles and the Non-Associative Cam Clay (NACC) model, exhibits intricate and realistic collapse dynamics. This simulation highlights the robustness, scalability, and efficiency of our method, achieving a runtime of 7.4s per frame.

The Material Point Method (MPM) has become a cornerstone of physics-based simulation, widely used in geomechanics and computer graphics for modeling phenomena such as granular flows, viscoelasticity, fracture mechanics, etc. Despite its versatility, the original MPM suffers from cell-crossing instabilities caused by discontinuities in particle-grid transfer kernels. Existing solutions mitigate these issues by adopting smoother shape functions, but at the cost of increased computational overhead due to larger kernel support. In this paper, we propose a novel C^2 -continuous compact kernel for MPM that achieves a unique balance between stability and computational efficiency. Our method integrates seamlessly with Affine Particle-In-Cell (APIC) and Moving Least Squares (MLS) MPM, while only doubling the number of grid nodes associated with each particle compared to linear kernels. At its core is an innovative dual-grid framework, which associates particles with grid nodes exclusively within the cells they occupy on two staggered grids, ensuring consistent and stable force computations. To further accelerate performance, we present a GPU-optimized implementation inspired by state-of-the-art massively parallel MPM techniques, achieving an additional $2\times$ speedup in G2P2G transfers over quadratic B-spline MPM. Comprehensive validation through unit tests, comparative studies, and stress tests demonstrates the efficacy of our approach in conserving both linear and angular momentum, handling stiff materials, and scaling efficiently for large-scale simulations. Our results highlight the transformative potential of compact, high-order kernels in advancing MPM’s capabilities for stable, high-performance simulations, paving the way for more computationally efficient applications in computer graphics and beyond.

CCS Concepts: • **Computing methodologies** → **Physical simulation.**

Additional Key Words and Phrases: material point methods, numerical analysis, elastoplasticity simulation, fracture simulation, physics-based animation

Authors’ Contact Information: Michael Liu, Carnegie Mellon University, USA, appledorem.g@gmail.com; Xinlei Wang, ZenusTech Inc., China, wxlwxl1993@zju.edu.cn; Minchen Li, Carnegie Mellon University, USA, minchernl@gmail.com.

1 Introduction

The Material Point Method (MPM), introduced by [Sulsky et al. \[1995\]](#) as an extension of the Particle-in-Cell (PIC) method [[Harlow 1962](#)], has found widespread applications in solid mechanics. It is widely used in fields such as geomechanics and computer graphics, including simulation of granular materials [[Chen et al. 2021](#); [Klár et al. 2016](#); [Yue et al. 2018](#); [Zhao et al. 2023](#)], viscoelastic materials [[Fang et al. 2019](#); [Su et al. 2021](#)], snow [[Gaume et al. 2018](#); [Stomakhin et al. 2013](#)], ductile fracture [[Wolper et al. 2020, 2019](#)], solid-fluid interactions [[Fang et al. 2020](#); [Fei et al. 2018, 2019, 2017](#)], frictional contact [[Guo et al. 2018](#); [Han et al. 2019](#); [Jiang et al. 2017](#)], phase change effects [[Ding et al. 2019](#); [Stomakhin et al. 2014](#); [Su et al. 2021](#)], and even combustion [[Kala et al. 2024](#)] and explosions [[Cao et al. 2022](#)]. For a complete survey, we refer the reader to [De Vaucorbeil et al. \[2020\]](#).

As a hybrid Lagrangian-Eulerian method, MPM employs Lagrangian particles to track the geometry of the simulation object while using a Eulerian background grid to compute forces and perform time integration. Alternatively, particles can be viewed as quadrature points, and the grid nodes represent the degrees of freedom (DOFs). In its original formulation, MPM adopted the piecewise linear particle-grid transfer kernel, similar to the kernel used in PIC. However, since MPM requires the gradient of the shape function to compute forces, linear kernels introduce discontinuities that cause numerical instability when particles move across grid cells - a phenomenon known as cell-crossing instability.

To address these challenges, various methods have been proposed. [Bardenhagen et al. \[2004\]](#) introduced the Generalized Interpolation Material Point (GIMP) method, which treats particles as volumes during particle-grid transfer, resulting in effective shape functions

derived from integrals of the linear kernel. [Sadeghirad et al. \[2011\]](#) further extended GIMP with Convected Particle Domain Interpolation (CPDI), which accounts for particle volume changes during transfer and improves accuracy, particularly for cases involving large tensile deformations and rotations. Similarly, [Wilson et al. \[2021\]](#) proposed dynamically splitting particles near cell boundaries into subparticles for transfer, achieving higher efficiency while mitigating cell-crossing issues, albeit with some loss of accuracy compared to GIMP.

Another approach involves directly using smoother shape functions. For example, [Steffen et al. \[2008\]](#) proposed using quadratic and cubic B-spline shape functions, which produce smoother forces and effectively reduce cell crossing instabilities. B-spline MPM is widely adopted in the graphics community due to their simplicity and effectiveness [\[Jiang et al. 2016\]](#). Building on this idea, [Moutsanidis et al. \[2020\]](#) introduced Isogeometric Analysis MPM (IGA-MPM), which uses non-uniform rational B-splines (NURBS) as shape functions. This approach provides additional flexibility, such as exact representations of conic sections and better preservation of symmetry in solutions.

An alternative strategy focuses on transferring stress from particles to the grid and then performing stress interpolation to calculate forces [\[Zhang et al. 2011\]](#). [Liang et al. \[2019\]](#) adapted this idea to a staggered grid, reducing the number of accumulation operations and improving computational efficiency.

In summary, most existing methods address cell-crossing instabilities by introducing smoother shape functions, which often come at the cost of much larger support regions and reduced computational performance. In contrast, we propose a novel C^2 -continuous compact kernel for particle-grid transfer that achieves a unique balance of stability and efficiency. Our approach is fully compatible with Affine Particle-In-Cell (APIC) [\[Jiang et al. 2015\]](#) and Moving Least Squares (MLS) MPM [\[Hu et al. 2018\]](#), effectively mitigating instabilities while only doubling the number of grid nodes associated with each particle compared to linear kernels.

To achieve this, we introduce a dual grid framework, where each particle is associated exclusively with the nodes of the cell it resides in on both grids. Furthermore, we develop a GPU-optimized implementation inspired by [Wang et al. \[2020\]](#), achieving an average $2\times$ speedup in the G2P2G transfer process compared to quadratic B-spline MPM. This additional improvement upon the highly optimized GPU MPM implementation enables efficient and stable simulations, even for complex and large-scale scenarios.

An extensive set of unit tests, comparative studies, and stress tests is performed to validate the efficacy of our method. These evaluations demonstrate its ability to conserve linear and angular momentum, handle stiff materials with robustness, and scale effectively for large-scale simulations. Our results highlight the transformative potential of the proposed approach for both research and practical applications in the field of MPM.

2 Background and Preliminaries

We follow [Jiang et al. \[2016\]](#); [Zong et al. \[2023\]](#) to derive the weak form of the governing equations for continuum simulation and briefly introduce the traditional MPM pipeline in this section.

2.1 Governing Equations

We denote $\Omega_0, \Omega_t \subset \mathbb{R}^3$ to be the material space and the world space, respectively. The material space and the world space match through an isomorphism at $t = 0$. For $t > 0$, we use the map $\phi : \Omega_0 \times (0, \infty) \rightarrow \mathbb{R}^3$ and $\phi(\mathbf{x}_{\Omega_0}, t) \in \Omega_t$ for $\mathbf{x}_{\Omega_0} \in \Omega_0$. We use subscripts to denote $\mathbf{x}_{\Omega_0}, \mathbf{x}_{\Omega_t}$ as the position in material space and world space at time t respectively. Then, following a Lagrangian formulation, we can model the dynamics of continuums through a density field $\rho_0 : \Omega_0 \times (0, \infty) \rightarrow \mathbb{R}$, a velocity field $\mathbf{v}_0 : \Omega_0 \times (0, \infty) \rightarrow \mathbb{R}^3$, and the following conservation of mass and conservation of momentum governing equations:

$$\begin{cases} \rho_0(\mathbf{x}_{\Omega_0}, t)J(\mathbf{x}_{\Omega_0}, t) = \rho_0(\mathbf{x}_{\Omega_0}, 0), \\ \rho_0(\mathbf{x}_{\Omega_0}, 0) \frac{\partial \mathbf{v}_0}{\partial t}(\mathbf{x}_{\Omega_0}, t) = \nabla_{\mathbf{x}_{\Omega_0}} \cdot \mathbf{P} + \rho_0(\mathbf{x}_{\Omega_0}, 0)\mathbf{g}, \end{cases}$$

where $J(\mathbf{x}_{\Omega_0}, t) = \det(\frac{\partial \phi}{\partial \mathbf{x}_{\Omega_0}}(\mathbf{x}_{\Omega_0}, t))$ and \mathbf{g} is the gravity. Moreover, let $\mathbf{F} = \frac{\partial \phi}{\partial \mathbf{x}_{\Omega_0}}(\mathbf{x}_{\Omega_0}, t)$ be the deformation gradient; then \mathbf{P} , the first Piola-Kirchhoff stress, is a function of the deformation gradient. We also define the Eulerian counterparts of ρ_0, \mathbf{v}_0 as ρ, \mathbf{v} .

2.2 Spatial and Temporal Discretization

In a practical context, we need to discretize the above equations. We first assume that we sample t with an interval Δt such that we evaluate our equations at time $t_n = n\Delta t$. We can approximate the Lagrangian velocity \mathbf{v}_0 and acceleration $\mathbf{a}_0 = \partial \mathbf{v}_0 / \partial t$ at time t_n using finite difference by $\frac{1}{\Delta t}(\mathbf{x}_{\Omega_{t_n}} - \mathbf{x}_{\Omega_{t_{n-1}}})$ and $\frac{1}{\Delta t}(\mathbf{v}_0(\cdot, t_{n+1}) - \mathbf{v}_0(\cdot, t_n))$, respectively. Here, we used Symplectic Euler, but the derivation also adapts to other time integrators. Then, assuming zero gravity and letting q_0 be any test functions in Ω_0 , we obtain the following weak form formulation in Ω_0 :

$$\begin{aligned} & \int_{\Omega_0} \rho_0(\cdot, 0) \frac{1}{\Delta t} (\mathbf{v}_0(\cdot, t_{n+1}) - \mathbf{v}_0(\cdot, t_n)) q_0(\cdot) d\mathbf{x}_{\Omega_0} \\ &= - \int_{\Omega_0} \mathbf{P} \nabla_{\mathbf{x}_{\Omega_0}} q_0 d\mathbf{x}_{\Omega_0}. \end{aligned} \quad (1)$$

We thus obtain a weak form formulation in Ω_{t_n} by a push-forward, which yields:

$$\begin{aligned} & \int_{\Omega_{t_n}} \rho(\cdot, t_n) \frac{1}{\Delta t} (\mathbf{v}(\cdot, t_{n+1}) - \mathbf{v}(\cdot, t_n)) q(\cdot) d\mathbf{x}_{\Omega_{t_n}} \\ &= - \int_{\Omega_{t_n}} \frac{1}{J} \mathbf{P} \mathbf{F}^T \nabla_{\mathbf{x}_{\Omega_{t_n}}} q d\mathbf{x}_{\Omega_{t_n}}, \end{aligned} \quad (2)$$

where $\mathbf{x}_{\Omega_{t_n}} = \phi(\mathbf{x}_{\Omega_0}, t_n)$ and q is the test function after push-forward. Then, if we use the position of particles \mathbf{x}_p as integration quadrature and B-spline kernels N with $w_{i,p,t_n} = N(\mathbf{x}_{p,t_n} - \mathbf{x}_i)$ where \mathbf{x}_i is the position of the background grid nodes. Then, by choosing proper test functions and using mass lumping, we can obtain the momentum update formula by the relation:

$$m_{i,t_n} (\mathbf{v}_{i,t_{n+1}} - \mathbf{v}_{i,t_n}) = -\Delta t \sum_p V_{p,0} \mathbf{P} \mathbf{F}^T \nabla w_{i,p,t_n}, \quad (3)$$

where $m_{i,t_n}, \mathbf{v}_{i,t_n}$ denotes the mass and velocity of node i at time t_n respectively, and $V_{p,0}$ denotes the volume of p at $t = 0$.

2.3 MPM Pipeline Overview

We provide an overview of the general pipeline for explicit MPM using a symplectic Euler time integrator. Each time step involves transferring quantities from particles to the background grid, performing computations on the grid to update velocities, and transferring the updated quantities back to the particles. The steps are as follows:

- (1) **Particle to Grid (P2G):** Particle masses are transferred to the grid using B-spline kernels, while momentum is transferred using either the PIC or APIC scheme.
- (2) **Grid Update:** The grid momentum is updated based on Equation 3, with grid-level boundary conditions applied as needed.
- (3) **Grid to Particle (G2P):** Particle velocities are interpolated from the grid using B-spline kernels. For the APIC scheme, an additional matrix is computed to capture the local affine deformations.
- (4) **Update Particle Deformation Gradient:** The deformation gradient $\mathbf{F}_{p,t_{n+1}}$ is updated using:

$$\mathbf{F}_{p,t_{n+1}} = (\mathbf{I} + \Delta t \sum_i \mathbf{v}_{i,t_{n+1}} (\nabla w_{i,p,t_n})^T) \mathbf{F}_{p,t_n},$$

where $\mathbf{v}_{i,t_{n+1}}$ is the grid velocity, $\nabla w_{i,p,t_n}$ is the gradient of the kernel weight, and Δt is the time step.

- (5) **Particle Advection:** Particle positions are updated by integrating the interpolated velocities.

Among these steps, the P2G operation is often the computational bottleneck of MPM, accounting for more than 90% of the total computation time. This is primarily because it involves a scattering operation, which requires careful parallelization and is often constrained by memory bandwidth and access patterns.

3 Compact-Kernel MPM

In this section, we introduce our novel compact kernel for the P2G and G2P processes, designed with a kernel radius of 2 and C^2 -continuity. Our kernel satisfies all critical properties of kernel functions (subsection 3.1). To apply this kernel effectively in a discrete setting, we propose a staggered dual-grid discretization (subsection 3.2), which forms the foundation of our compact-kernel (CK) MPM (subsection 3.3). We further establish the theoretical foundation of our CK-MPM by proving its conservation properties for linear and angular momentum when combined with widely-used particle-grid transfer schemes such as APIC (subsection 3.4) and MLS-MPM (subsection 3.5), highlighting its versatility and potential for high-performance continuum simulations. The symbols used in our derivation can be found in Table 1.

3.1 Smoothing Linear B-Spline Kernel

In designing a new kernel function $\mathcal{K}(x)$ with a radius of 2 for MPM, our main intuition is to modify the linear B-spline kernel by adding a smoothing function $\mathcal{S}(x)$, that is,

$$\mathcal{K}(x) = 1 - |x| + \mathcal{S}(x),$$

so that the following properties are satisfied:

- (1) **Normalization:** $\int_{\mathbb{R}} \mathcal{K}(x) dx = 1.$

Table 1. Notation.

Symbol	Description
Δx	Uniform, scalar distance between adjacent grid nodes
Δt	Time step size
$\mathbf{x}^{\alpha_1 \dots \alpha_p}$ $\beta_1 \dots \beta_q$	A p -times contravariant, q -times covariant tensor
δ	Kronecker delta tensor
ε	Levi-Civita symbol for cross product
$\text{sgn}(x)$	The sign function

- (2) **Monotonicity:** $\begin{cases} \mathcal{K}(a) > \mathcal{K}(b), & \text{if } 0 \leq a < b \\ \mathcal{K}(a) > \mathcal{K}(b), & \text{if } 0 \geq a > b \end{cases}$
- (3) **Non-Negativity:** $\forall x \in \mathbb{R}, \mathcal{K}(x) \geq 0.$
- (4) **Compactness:** $|x| \geq 1 \implies \mathcal{K}(x) = 0.$
- (5) **Convergence to Dirac Delta:** $\lim_{h \rightarrow 0} \mathcal{K}(\frac{x}{h}) = \delta(\frac{x}{h}).$
- (6) **Smoothness:** $\mathcal{K}(x)$ is C^2 -Continuous.

We observe that the original linear B-spline kernel already satisfies all above properties except item 6. This indicates that our smoothing function should at least satisfy that:

$$\int_{\mathbb{R}} \mathcal{S}(x) dx = 0, \quad \text{and} \quad \mathcal{S}(0) = \mathcal{S}(1) = \mathcal{S}(-1) = 0.$$

Note that the condition $\mathcal{S}(0) = 0$ is an artificial choice to resemble the behavior of linear kernel, and the conditions $\mathcal{S}(-1) = \mathcal{S}(1) = 0$ ensures our kernel has radius 2. Although it is possible to construct a kernel with smaller radius, we deliberately omit such construction since it is not applicable in the discrete case as it associate a particle with only one grid node. From the property on the right above, it is natural to consider periodic functions for potential candidates of $\mathcal{S}(x)$. Moreover, since $\{\sin(n\pi x), \cos(n\pi x) \mid \forall n \in \mathbb{N}\}$ forms a basis of $\mathcal{L}^2[-1, 1]$ (the Lebesgue space of square integrable functions defined on the $[-1, 1]$), we can fourier transform the function $\mathcal{S}(x) \in \mathcal{L}^2[-1, 1]$ into such basis and obtain:

$$\mathcal{S}(x) = \sum_{n=0}^{\infty} a_n \sin(n\pi x) + \sum_{m=0}^{\infty} b_m \cos(m\pi x),$$

where $a_n, b_m \in \mathbb{R}, \forall n, m \in \mathbb{N}$.

To ensure $\mathcal{S}(0) = 0$, we can set $\forall m \in \mathbb{N}, b_m = 0$, and we have

$$\mathcal{S}(x) = \sum_{n=0}^{\infty} a_n \sin(n\pi x).$$

To smooth out the non-differentiability of the linear B-spline kernel at $x = 0$, we first observe that the derivative of the linear B-spline kernel when $x \neq 0$ could be written as $-\text{sgn}(x)$, where sgn denotes the sign function. Since $\mathcal{K}(x)$ should reach the maximum value of 1 at $x = 0$, it should have a derivative of 0 at $x = 0$, which requires $\lim_{x \rightarrow 0^-} \frac{d}{dx} \mathcal{S}(x) = -1$ and $\lim_{x \rightarrow 0^+} \frac{d}{dx} \mathcal{S}(x) = 1$. With a slight abuse of notation, we replace the x in the decomposition of $\mathcal{S}(x)$ with $|x|$, leading us to observe that:

$$\frac{d}{dx} \mathcal{S}(x) = \frac{d}{dx} \left(\sum_{n=0}^{\infty} a_n \sin(n\pi|x|) \right) = \pi \text{sgn}(x) \sum_{n=0}^{\infty} a_n n \cos(n\pi|x|).$$

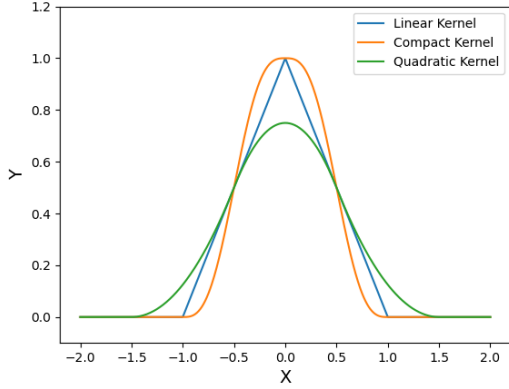


Fig. 2. Plot of linear, quadratic B-spline, and our compact kernel functions.

For the above function, if we restrict $\pi(\sum_{n=0}^{\infty} a_n n) = 1$, we have:

$$\begin{aligned} & \lim_{x \rightarrow 0^-} \frac{d}{dx} \mathcal{S}(x) \\ &= \lim_{x \rightarrow 0^-} \pi \operatorname{sgn}(x) \sum_{n=0}^{\infty} a_n \cos(n\pi x) \\ &= (\pi \sum_{n=0}^{\infty} a_n n) \lim_{x \rightarrow 0^-} \operatorname{sgn}(x) \\ &= -1, \end{aligned}$$

where it can be similarly shown that $\lim_{x \rightarrow 0^+} \frac{d}{dx} \mathcal{S}(x) = 1$, and they now nicely cancel out the unequal derivatives of the original linear B-spline kernel at $x = 0$.

To ensure C^2 -continuity of $\mathcal{K}(x)$, we also need its gradient to be smooth at $|x| = 1$. For $x = 1$, we observe that $\frac{d}{dx} \mathcal{S}(x)|_{x=1} = \pi \sum_{n=0}^{\infty} (-1)^n a_n n$ is a non-convergent sequence. We therefore pick $a_n = 0$ for all odd n so that it reduces to $\pi \sum_{n=0}^{\infty} 2a_{2n} n$, which still converges under the restriction $\pi(\sum_{n=0}^{\infty} a_n n) = 1$, and so can be used to cancel out the derivative of linear B-spline functions, similar to when $x = 0$ discussed above. The case for $x = -1$ is similar, and we reach a reduced form of the kernel function $\mathcal{S}(x)$, satisfying all required properties:

$$\mathcal{S}(x) = \sum_{n=0}^{\infty} 2a_{2n} n \sin(2n\pi|x|). \quad (4)$$

For computational efficiency, we simply choose $a_n = 0$ for all n except $n = 2$. Hence, our final kernel function in the 1-D setting is (Figure 2):

$$\mathcal{K}_1(x) = 1 - |x| + \frac{1}{2\pi} \sin(2\pi|x|). \quad (5)$$

3.2 Discrete Compact Kernel

We now examine the property of our compact kernel in discrete settings. We define $\mathcal{K} : \mathbb{R} \rightarrow \mathbb{R}$ by:

$$\mathcal{K}(x^\alpha) = \prod_{\beta=0}^2 \mathcal{K}_1(x^\beta) \quad (6)$$

For $\mathcal{K}(x)$ to be an interpolation kernel, it must satisfy the following two properties to ensure 1st-order accuracy:

$$\sum_i \mathcal{K}\left(\frac{x_p^\alpha - x_i^\alpha}{\Delta x}\right) = 1 \quad (7)$$

$$\sum_i x_i^\alpha \mathcal{K}\left(\frac{x_p^\beta - x_i^\beta}{\Delta x}\right) = x^\alpha \quad (8)$$

To show that $\mathcal{K}(x)$ satisfies Equation 7, we consider the grid nodes that are associated with x_p^α . Since the kernel has a radius of 2, there are eight grid nodes in total that are associated with x_p^α . For $0 \leq s, t, u \leq 1$, we denote $x_{B_p}^\alpha(s, t, u)$ to be the grid nodes, which contain x_p^α , where s, t, u denotes the nodal offset in the x, y, z -axis direction from the bottom left grid node $x_{B_p}^\alpha(0, 0, 0)$. We observe that:

$$\begin{aligned} & \sum_i \mathcal{K}\left(\frac{x_p^\alpha - x_i^\alpha}{\Delta x}\right) \\ &= \sum_{s=0}^1 \sum_{t=0}^1 \sum_{u=0}^1 \mathcal{K}\left(\frac{x_p^\alpha - x_{B_p}^\alpha(s, t, u)}{\Delta x}\right) \\ &= \sum_{s=0}^1 \sum_{t=0}^1 \sum_{u=0}^1 \prod_{\alpha=0}^2 \mathcal{K}_1\left(\frac{x_p^\alpha - x_{B_p}^\alpha(s, t, u)}{\Delta x}\right) \\ &= \sum_{s=0}^1 \sum_{t=0}^1 \left(\sum_{u=0}^1 \mathcal{K}_1\left(\frac{x_p^2 - x_{B_p}^2(s, t, u)}{\Delta x}\right) \prod_{\alpha=0}^1 \mathcal{K}_1\left(\frac{x_p^\alpha - x_{B_p}^\alpha(s, t, 0)}{\Delta x}\right) \right) \\ &= \sum_{s=0}^1 \sum_{t=0}^1 \left(\left(\mathcal{K}_1\left(\frac{x_p^2 - x_{B_p}^2(s, t, u)}{\Delta x}\right) + \mathcal{K}_1\left(\frac{x_p^2 - x_{B_p}^2(s, t, u+1)}{\Delta x}\right) \right) \right. \\ & \quad \left. \prod_{\alpha=0}^1 \mathcal{K}_1\left(\frac{x_p^\alpha - x_{B_p}^\alpha(s, t, 0)}{\Delta x}\right) \right), \end{aligned}$$

since $x_{B_p}^0(s, t, u)$ and $x_{B_p}^1(s, t, u)$ are not affected by u and $x_{B_p}^0(s, t, u)$ is not affected by t . Now, recall our previous definition of \mathcal{K}_1 , we see that the following equation holds:

$$\mathcal{K}_1(x) + \mathcal{K}_1(1-x) = 1 \quad (9)$$

which resembles the behavior of linear kernels. Hence, we have:

$$\begin{aligned} &= \sum_{s=0}^1 \sum_{t=0}^1 \prod_{\alpha=0}^1 \mathcal{K}_1\left(\frac{x_p^\alpha - x_{B_p}^\alpha(s, t, 0)}{\Delta x}\right) \\ &= \sum_{s=0}^1 \mathcal{K}_1\left(\frac{x_p^0 - x_{B_p}^0(s, 0, 0)}{\Delta x}\right) \left(\sum_{t=0}^1 \mathcal{K}_1\left(\frac{x_p^1 - x_{B_p}^1(s, 0, 0)}{\Delta x}\right) \right) \\ &= \sum_{s=0}^1 \mathcal{K}_1\left(\frac{x_p^0 - x_{B_p}^0(s, 0, 0)}{\Delta x}\right) \\ &= 1 \end{aligned}$$

For the property in Equation 8, it does not hold in general. To achieve this property in the discrete setting, we introduce a dual-grid system. Consider three grids $\{\mathcal{G}_0, \mathcal{G}_-, \mathcal{G}_+\}$ where \mathcal{G}_0 denotes an initial grid and $\mathcal{G}_-, \mathcal{G}_+$ denote grids with an offset of $+\frac{1}{4}\Delta, -\frac{1}{4}\Delta x$ in all axes to \mathcal{G}_0 respectively (note that we may use $\mathcal{G}_{\pm 1} \cong \mathcal{G}_{\pm}$

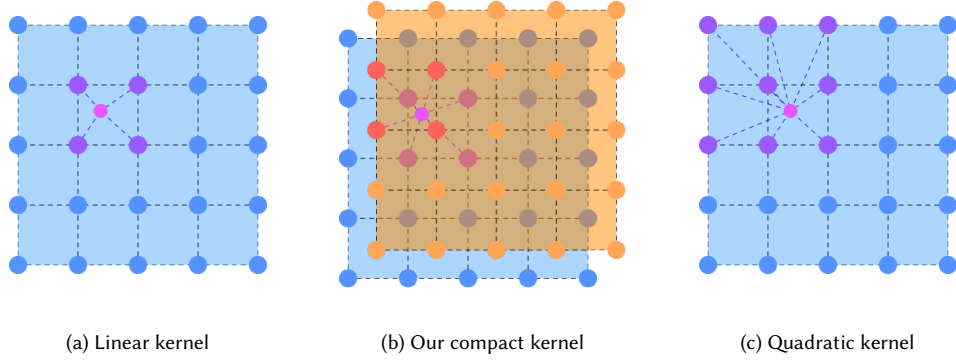


Fig. 3. Comparison of interpolation patterns of different kernels in 2D.

interchangeably). We will show that in the dual grid system, the property in Equation 8 can be achieved.

We first restate the two properties (Equation 7 and Equation 8) in the new dual grid setting as:

$$\frac{1}{2} \sum_{k \in \{\pm 1\}} \sum_i \mathcal{K}\left(\frac{\mathbf{x}_{p, \mathcal{G}_0}^\alpha - \mathbf{x}_{i, \mathcal{G}_k}^\alpha}{\Delta x}\right) = 1 \quad (10)$$

$$\frac{1}{2} \sum_{k \in \{\pm 1\}} \sum_i \mathbf{x}_{i, \mathcal{G}_k}^\alpha \mathcal{K}\left(\frac{\mathbf{x}_{\mathcal{G}_0}^\beta - \mathbf{x}_{i, \mathcal{G}_k}^\beta}{\Delta x}\right) = \mathbf{x}_{\mathcal{G}_0}^\alpha \quad (11)$$

where $\mathbf{x}_{\dots, \mathcal{G}_k}^v$ indicates it is a position in grid \mathcal{G}_k . We can compute the position in grid \mathcal{G}_k through the canonical transformation function:

$$\mathbf{x}_{\mathcal{G}_k}^v = \mathbf{x}_{\mathcal{G}_0}^v - k \frac{1}{4} \Delta x \mathbf{e}^v \quad (12)$$

where \mathbf{e}^v denotes the vector of 1 in all dimensions. It is trivial to see that Equation 10 holds since it follows directly from Equation 7.

With the above transformation function and Figure 3, we note that the set of associated grid nodes with $\mathbf{x}_{\mathcal{G}_0}^v$ is located on the vertices of a pair of staggered cells. We adopt previous notation with slight modifications that $\mathbf{x}_{B(s,t,u), \mathcal{G}_k}$ denotes the grid nodes in grid \mathcal{G}_k that are associated with $\mathbf{x}_{\mathcal{G}_0}$ with a grid-level offset (s, t, u) on x, y, z -axis respectively to the bottom left grid nodes $\mathbf{x}_{B(0,0,0), \mathcal{G}_k}$. We thus observe:

$$\begin{aligned} & \frac{1}{2} \sum_{k \in \{\pm 1\}} \sum_i \mathbf{x}_{i, \mathcal{G}_k}^\alpha \mathcal{K}\left(\frac{\mathbf{x}_{\mathcal{G}_0}^\beta - \mathbf{x}_{i, \mathcal{G}_k}^\beta}{\Delta x}\right) \\ &= \frac{1}{2} \sum_{k \in \{\pm 1\}} \sum_{s=0}^1 \sum_{t=0}^1 \sum_{u=0}^1 \mathbf{x}_{B(s,t,u), \mathcal{G}_k}^\alpha \mathcal{K}\left(\frac{\mathbf{x}_{\mathcal{G}_0}^\beta - \mathbf{x}_{B(s,t,u), \mathcal{G}_k}^\beta}{\Delta x}\right) \\ &= \frac{1}{2} \sum_{k \in \{\pm 1\}} \sum_{s=0}^1 \sum_{t=0}^1 \left(\mathbf{x}_{B(s,t,0), \mathcal{G}_k}^\alpha \mathcal{K}\left(\frac{\mathbf{x}_{\mathcal{G}_0}^\beta - \mathbf{x}_{B(s,t,0), \mathcal{G}_k}^\beta}{\Delta x}\right) \right. \\ & \quad \left. + (\delta_2^\alpha \Delta x + \mathbf{x}_{B(s,t,0), \mathcal{G}_k}^\alpha) \mathcal{K}\left(\frac{\mathbf{x}_{\mathcal{G}_0}^\beta - \mathbf{x}_{B(s,t,0), \mathcal{G}_k}^\beta - \delta_2^\beta \Delta x}{\Delta x}\right) \right) \\ &= \frac{1}{2} \sum_{k \in \{\pm 1\}} \sum_{s=0}^1 \sum_{t=0}^1 \left(\mathbf{x}_{B(s,t,0), \mathcal{G}_k}^\alpha \prod_{v=0}^1 \mathcal{K}_1\left(\frac{\mathbf{x}_{\mathcal{G}_0}^v - \mathbf{x}_{B(s,t,0), \mathcal{G}_k}^v}{\Delta x}\right) \right. \\ & \quad \left. + \delta_2^\alpha \Delta x \mathcal{K}\left(\frac{\mathbf{x}_{\mathcal{G}_0}^\beta - \mathbf{x}_{B(s,t,0), \mathcal{G}_k}^\beta - \delta_2^\beta \Delta x}{\Delta x}\right) \right) \\ &= \frac{1}{2} \sum_{k \in \{\pm 1\}} \sum_{s=0}^1 \left(\mathbf{x}_{B(s,0,0), \mathcal{G}_k}^\alpha \mathcal{K}_1\left(\frac{\mathbf{x}_{\mathcal{G}_0}^0 - \mathbf{x}_{B(s,0,0), \mathcal{G}_k}^0}{\Delta x}\right) \right. \\ & \quad \left. + \delta_1^\alpha \Delta x \prod_{v=0}^1 \mathcal{K}_1\left(\frac{\mathbf{x}_{\mathcal{G}_0}^v - \mathbf{x}_{B(s,0,0), \mathcal{G}_k}^v - \delta_1^v \Delta x}{\Delta x}\right) \right. \\ & \quad \left. + \delta_2^\alpha \Delta x \prod_{\beta \in \{0,2\}} \mathcal{K}\left(\frac{\mathbf{x}_{\mathcal{G}_0}^\beta - \mathbf{x}_{B(s,0,0), \mathcal{G}_k}^\beta - \delta_2^\beta \Delta x}{\Delta x}\right) \right) \\ &= \frac{1}{2} \sum_{k \in \{\pm 1\}} \left(\mathbf{x}_{B(0,0,0), \mathcal{G}_k}^\alpha + \delta_0^\alpha \Delta x \mathcal{K}_1\left(\frac{\mathbf{x}_{\mathcal{G}_0}^0 - \mathbf{x}_{B(0,0,0), \mathcal{G}_k}^0 - \Delta x}{\Delta x}\right) \right. \\ & \quad \left. + \delta_1^\alpha \Delta x \mathcal{K}_1\left(\frac{\mathbf{x}_{\mathcal{G}_0}^v - \mathbf{x}_{B(0,0,0), \mathcal{G}_k}^v - \Delta x}{\Delta x}\right) \right. \\ & \quad \left. + \delta_2^\alpha \Delta x \mathcal{K}\left(\frac{\mathbf{x}_{\mathcal{G}_0}^2 - \mathbf{x}_{B(0,0,0), \mathcal{G}_k}^2}{\Delta x}\right) \right) \\ &= \mathbf{x}_{B(0,0,0), \mathcal{G}_0}^\alpha + \frac{1}{2} \sum_{k \in \{\pm 1\}} \sum_{\mu=0}^2 \delta_\mu^\alpha \Delta x \mathcal{K}_1\left(\frac{\mathbf{x}_{\mathcal{G}_0}^\mu - \mathbf{x}_{B(0,0,0), \mathcal{G}_k}^\mu - \Delta x}{\Delta x}\right) \end{aligned}$$

To finalize our proof for Equation 11, it suffices to show that:

$$\frac{1}{2} \sum_{k \in \{\pm 1\}} \Delta x \mathcal{K}_1 \left(\frac{\mathbf{x}_{\mathcal{G}_0}^\mu - \mathbf{x}_{B(0,0,0),\mathcal{G}_k}^\mu - \Delta x}{\Delta x} \right) = \mathbf{x}_{\mathcal{G}_0}^\mu - \mathbf{x}_{B(0,0,0),\mathcal{G}_0}^\mu \quad (13)$$

for each $\mu \in \{0, 1, 2\}$. We first note that by our definition, it must be true that:

$$\begin{aligned} 0 &\leq \mathbf{x}_{\mathcal{G}_0}^\mu - \mathbf{x}_{B(0,0,0),\mathcal{G}_k}^\mu \leq \Delta x \\ \implies -1 &\leq \frac{\mathbf{x}_{\mathcal{G}_0}^\mu - \mathbf{x}_{B(0,0,0),\mathcal{G}_k}^\mu - \Delta x}{\Delta x} \leq 0 \end{aligned}$$

Hence, we have:

$$\begin{aligned} &\frac{1}{2} \sum_{k \in \{\pm 1\}} \Delta x \mathcal{K}_1 \left(\frac{\mathbf{x}_{\mathcal{G}_0}^\mu - \mathbf{x}_{B(0,0,0),\mathcal{G}_k}^\mu - \Delta x}{\Delta x} \right) \\ &= \frac{1}{2} \sum_{k \in \{\pm 1\}} \Delta x \mathcal{K}_1 \left(\frac{\mathbf{x}_{\mathcal{G}_0}^\mu - \mathbf{x}_{B(0,0,0),\mathcal{G}_0}^\mu + \frac{k\Delta x}{4} - \Delta x}{\Delta x} \right) \\ &= \frac{\Delta x}{2} \left(2 + \left(\frac{\mathbf{x}_{\mathcal{G}_0}^\mu - \mathbf{x}_{B(0,0,0),\mathcal{G}_0}^\mu}{\Delta x} - \frac{5}{4} \right) + \left(\frac{\mathbf{x}_{\mathcal{G}_0}^\mu - \mathbf{x}_{B(0,0,0),\mathcal{G}_0}^\mu}{\Delta x} - \frac{3}{4} \right) \right. \\ &\quad \left. - \frac{1}{2\pi} \sin \left(2\pi \left(\frac{\mathbf{x}_{\mathcal{G}_0}^\mu - \mathbf{x}_{B(0,0,0),\mathcal{G}_0}^\mu}{\Delta x} - \frac{5}{4} \right) \right) \right. \\ &\quad \left. - \frac{1}{2\pi} \sin \left(2\pi \left(\frac{\mathbf{x}_{\mathcal{G}_0}^\mu - \mathbf{x}_{B(0,0,0),\mathcal{G}_0}^\mu}{\Delta x} - \frac{3}{4} \right) \right) \right) \\ &= \mathbf{x}_{\mathcal{G}_0}^\mu - \mathbf{x}_{B(0,0,0),\mathcal{G}_0}^\mu \end{aligned}$$

This concludes the proof for Equation 11.

3.3 Compact-Kernel MPM

With the introduction of the dual-grid system, we now present a variation of the traditional MPM pipeline. First, we introduce a modified version of the PIC scheme and demonstrate its linear momentum conservation properties. In subsection 3.4 and subsection 3.5, we further extend the PIC pipeline to include additional formulations, demonstrating angular momentum conservation.

In all the following schemes, particle positions are stored in grid \mathcal{G}_0 , while the other two grids are treated as offset grids. For clarity and brevity, we define the notation $w_{i,p,k,t_n} := \mathcal{K} \left(\frac{\mathbf{x}_{i,\mathcal{G}_k,t_n}^\beta - \mathbf{x}_{p,\mathcal{G}_0,t_n}^\beta}{\Delta x} \right)$ to represent the kernel function.

3.3.1 Transfer to grid. For mass and momentum, the new particle-to-grid transfer equations in the dual grid system are:

$$m_{i,\mathcal{G}_k,t_n} = \sum_p w_{i,p,\mathcal{G}_k,t_n} m_p \quad (14)$$

$$m_{i,\mathcal{G}_k,t_n} \tilde{\mathbf{v}}_{i,\mathcal{G}_k,t_n}^\alpha = \sum_p w_{i,p,\mathcal{G}_k,t_n} m_p \mathbf{v}_{p,t_n}^\alpha \quad (15)$$

We are thus distributing the particle information onto both grids.

3.3.2 Compute force. We first obtain the first Piola-Kirchoff stress on grid \mathcal{G}_0 :

$$(\mathbf{P}_{p,\mathcal{G}_0,t_n})_\beta^\alpha = \frac{\partial \Psi}{\partial (\mathbf{F})_\alpha^\beta} (\mathbf{F}_{p,\mathcal{G}_0,t_n}) \quad (16)$$

Then, we can compute the force on grid by:

$$\mathbf{f}_{i,\mathcal{G}_k,t_n}^\alpha = \sum_p V_p (\mathbf{P}_{p,\mathcal{G}_0,t_n})_\beta^\alpha (\mathbf{F}_{p,\mathcal{G}_0,t_n})_\beta^v (\nabla w_{i,p,\mathcal{G}_k,t_n})^v \quad (17)$$

3.3.3 Grid update. We then update two grids independently:

$$m_{i,\mathcal{G}_k,t_n} \tilde{\mathbf{v}}_{i,\mathcal{G}_k,t_n}^\alpha = m_{i,\mathcal{G}_k,t_n} \mathbf{v}_{i,\mathcal{G}_k,t_n}^\alpha + \Delta t \mathbf{f}_{i,\mathcal{G}_k,t_n}^\alpha \quad (18)$$

for each $k \in \{\pm 1\}$.

3.3.4 Transfer to particles. When transferring to particles, we gather information from both grids as implied by the proof of Equation 11:

$$\mathbf{v}_{p,t_n}^\alpha = \frac{1}{2m_p} \sum_{k \in \{\pm 1\}} \sum_i w_{i,p,\mathcal{G}_k,t_n} m_{i,\mathcal{G}_k,t_n} \tilde{\mathbf{v}}_{i,\mathcal{G}_k,t_n}^\alpha \quad (19)$$

3.3.5 Update deformation gradient. To compute forces in PIC scheme, we calculate the covariant derivative of velocity from both grids:

$$\frac{\partial \mathbf{v}_{p,\mathcal{G}_0,t_n}^\alpha}{\partial \mathbf{x}_{p,\mathcal{G}_0,t_n}^\beta} = \frac{1}{2} \sum_{k \in \{-1,+1\}} \sum_i \tilde{\mathbf{v}}_{i,\mathcal{G}_k,t_n}^\alpha ((\nabla w_{i,p,k,t_n})^T)_\beta \quad (20)$$

And, we update deformation gradient as in the traditional MPM pipeline:

$$(\mathbf{F}_{p,\mathcal{G}_0,t_n})_\beta^\alpha = (\delta_v^\alpha + \Delta t \frac{\partial \mathbf{v}_{p,\mathcal{G}_0,t_n}^\alpha}{\partial \mathbf{x}_{p,\mathcal{G}_0,t_n}^\beta}) (\mathbf{F}_{p,\mathcal{G}_0,t_n})_\beta^v \quad (21)$$

In Appendix A, we prove that our CK-MPM with the PIC particle-grid transfer scheme conserves linear momentum.

3.4 Compatibility with APIC

The Affine Particle-In-Cell (APIC) [Jiang et al. 2015] method is widely recognized for its ability to preserve angular momentum by incorporating affine matrices to capture additional particle information. In this subsection, we first present the adapted formulation of APIC within our dual-grid system. Subsequently, we demonstrate that this adapted formulation conserves angular momentum.

3.4.1 Particle-to-Grid Transfer. In the additional matrix $\mathcal{D}_{p,\mathcal{G}_0,t_n}$ plays an essential role in APIC for angular momentum conservation by capturing the affine motion of particles. In our CK-MPM, the computation of $\mathcal{D}_{p,\mathcal{G}_0,t_n}$ is adapted as follows:

$$\begin{aligned} (\mathcal{D}_{p,\mathcal{G}_0,t_n})_\beta^\alpha &= \frac{1}{2} \sum_{k \in \{\pm 1\}} \sum_i w_{i,p,\mathcal{G}_k,t_n} (\mathbf{x}_{i,\mathcal{G}_k,t_n}^\alpha - \mathbf{x}_{p,\mathcal{G}_0,t_n}^\alpha) \\ &\quad (\mathbf{x}_{i,\mathcal{G}_k,t_n}^\beta - \mathbf{x}_{p,\mathcal{G}_0,t_n}^\beta)^T \end{aligned}$$

Then, the particle-to-grid transfer in the dual grid system is similar to the PIC setting:

$$\begin{aligned} m_{i,\mathcal{G}_k,t_n} \mathbf{v}_{i,\mathcal{G}_k,t_n}^\alpha &= \\ \sum_p w_{i,p,\mathcal{G}_k,t_n} m_p (\mathbf{v}_{p,t_n}^\alpha + (\mathbf{B}_{p,t_n})_v^\alpha ((\mathcal{D}_{p,t_n})^{-1})_v^\beta (\mathbf{x}_{i,\mathcal{G}_k,t_n}^\beta - \mathbf{x}_{p,t_n}^\beta)) &\quad (22) \end{aligned}$$

3.4.2 *Grid-to-particle Transfer.* Another core component of the APIC scheme is the computation of the matrix $\mathbf{B}_{p, \mathcal{G}_0, t^{n+1}}$. In our dual-grid system, we define the computation as:

$$\begin{aligned} (\mathbf{B}_{p, \mathcal{G}_0, t^{n+1}})_{\beta}^{\alpha} = & \\ \frac{1}{2} \sum_{k \in \{\pm 1\}} \sum_i w_{i, p, \mathcal{G}_k, t_n} \tilde{\mathbf{v}}_{i, \mathcal{G}_k, t^{n+1}}^{\alpha} ((\mathbf{x}_{i, \mathcal{G}_k, t_n} - \mathbf{x}_{p, \mathcal{G}_0, t_n})^T)_{\beta}. & \quad (23) \end{aligned}$$

The rest of the pipeline and formulation will follow the same form as shown above in the PIC scheme. We prove that our CK-MPM will also conserve total linear and angular momentum with the adopted APIC scheme in [Appendix B](#).

3.5 Compatibility with MLS-MPM

The Moving Least Squares (MLS) MPM method provides an accurate and efficient approximation of the traditional MPM algorithm and is fully compatible with APIC. Here, we demonstrate that our CK-MPM algorithm is also compatible with the MLS scheme, allowing it to benefit from the performance acceleration offered by MLS.

Using the dual-grid notation introduced earlier, let us consider two sets of samples of a scalar function $u : \mathbb{R}^3 \rightarrow \mathbb{R}$, taken at locations $\mathbf{x}_{i, \mathcal{G}_-}$ and $\mathbf{x}_{i, \mathcal{G}_+}$. Our goal is to approximate u in a local neighborhood around a fixed point \mathbf{x} . This is achieved by performing a polynomial least-squares fit.

Let $\mathbf{P} : \mathbb{R}^3 \rightarrow \mathbb{R}^d$ denote the vector of polynomial basis functions. We aim to approximate the value of u at a query point $\mathbf{z}_{\mathcal{G}_0}$ near $\mathbf{x}_{\mathcal{G}_0}$ using the following formulation:

$$u(\mathbf{z}_{\mathcal{G}_0}) = (\mathbf{P}^T(\mathbf{z}_{\mathcal{G}_0}^{\alpha} - \mathbf{x}_{\mathcal{G}_0}^{\alpha}))_{\beta} \mathbf{c}^{\beta}(\mathbf{x}) \quad (24)$$

where $\mathbf{c}^{\beta}(\mathbf{x})$ are the coefficients obtained from the least-squares fit.

Following the element-free Galerkin (EFG) method, we also aim to minimize a functional of the following form:

$$\begin{aligned} \mathcal{J}_{\mathbf{x}_{\mathcal{G}_0}}(\mathbf{c}) & \\ = \frac{1}{2} \sum_{k \in \{\pm 1\}} \sum_i \mathcal{K}(\mathbf{x}_{\mathcal{G}_0} - \mathbf{x}_{i, \mathcal{G}_k}) (\mathbf{P}^T(\mathbf{x}_{i, \mathcal{G}_k} - \mathbf{x}_{\mathcal{G}_0}) \mathbf{c}(\mathbf{x}_{\mathcal{G}_0}) - u_i)^2 & \quad (25) \end{aligned}$$

We find that minimum of \mathbf{c} with a functional derivative:

$$\begin{aligned} & \frac{\partial \mathcal{J}_{\mathbf{x}_{\mathcal{G}_0}}}{\partial \mathbf{c}^{\alpha}} \delta^{\beta} \\ = \frac{\partial \mathcal{J}_{\mathbf{x}_{\mathcal{G}_0}}(\mathbf{c} + \tau \delta)}{\partial \tau} \Big|_{\tau=0} & \\ = \frac{\partial}{\partial \tau} \left(\frac{1}{2} \sum_{k \in \{\pm 1\}} \sum_i \mathcal{K}(\mathbf{x}_{i, \mathcal{G}_k} - \mathbf{x}_{\mathcal{G}_0}) (\mathbf{P}^T(\mathbf{x}_{i, \mathcal{G}_k} - \mathbf{x}_{\mathcal{G}_0}) (\mathbf{c} + \tau \delta)(\mathbf{x}_{\mathcal{G}_0}) - u_i)^2 \right) \Big|_{\tau=0} & \\ = \frac{1}{2} \sum_{k \in \{\pm 1\}} \sum_i \mathcal{K}(\mathbf{x}_{i, \mathcal{G}_k} - \mathbf{x}_{\mathcal{G}_0}) & \\ \frac{\partial}{\partial \tau} \left((\mathbf{P}^T(\mathbf{x}_{i, \mathcal{G}_k} - \mathbf{x}_{\mathcal{G}_0}) (\mathbf{c} + \tau \delta)(\mathbf{x}_{\mathcal{G}_0}) - u_i)^2 \right) \Big|_{\tau=0} & \\ = \frac{1}{2} \sum_{k \in \{\pm 1\}} \sum_i \mathcal{K}(\mathbf{x}_{i, \mathcal{G}_k} - \mathbf{x}_{\mathcal{G}_0}) & \\ \left(2\mathbf{P}^T(\mathbf{x}_{i, \mathcal{G}_k} - \mathbf{x}_{\mathcal{G}_0}) \mathbf{c} \mathbf{P}^T(\mathbf{x}_{i, \mathcal{G}_k} - \mathbf{x}_{\mathcal{G}_0}) - 2\mathbf{P}^T(\mathbf{x}_{i, \mathcal{G}_k} - \mathbf{x}_{\mathcal{G}_0}) u_i \right) \delta & \end{aligned}$$

To reach $\frac{\partial \mathcal{J}_{\mathbf{x}_{\mathcal{G}_0}}}{\partial \mathbf{c}^{\alpha}} \delta^{\alpha} = 0$, as δ is arbitrary, we need:

$$\begin{aligned} & \frac{1}{2} \sum_{k \in \{\pm 1\}} \sum_i \mathcal{K}(\mathbf{x}_{i, \mathcal{G}_k} - \mathbf{x}_{\mathcal{G}_0}) \\ & \left(2\mathbf{P}^T(\mathbf{x}_{i, \mathcal{G}_k} - \mathbf{x}_{\mathcal{G}_0}) \mathbf{c} \mathbf{P}^T(\mathbf{x}_{i, \mathcal{G}_k} - \mathbf{x}_{\mathcal{G}_0}) - 2\mathbf{P}^T(\mathbf{x}_{i, \mathcal{G}_k} - \mathbf{x}_{\mathcal{G}_0}) u_i \right) \\ & = 0 \\ \Rightarrow \frac{1}{2} \sum_{k \in \{\pm 1\}} \sum_i \mathcal{K}(\mathbf{x}_{i, \mathcal{G}_k} - \mathbf{x}_{\mathcal{G}_0}) \mathbf{P}^T(\mathbf{x}_{i, \mathcal{G}_k} - \mathbf{x}_{\mathcal{G}_0}) \mathbf{c} & \\ \mathbf{P}^T(\mathbf{x}_{i, \mathcal{G}_k} - \mathbf{x}_{\mathcal{G}_0}) & \\ = \frac{1}{2} \sum_{k \in \{\pm 1\}} \sum_i \mathcal{K}(\mathbf{x}_{i, \mathcal{G}_k} - \mathbf{x}_{\mathcal{G}_0}) \mathbf{P}^T(\mathbf{x}_{i, \mathcal{G}_k} - \mathbf{x}_{\mathcal{G}_0}) u_i & \\ \Rightarrow \frac{1}{2} \sum_{k \in \{\pm 1\}} \sum_i \mathcal{K}(\mathbf{x}_{i, \mathcal{G}_k} - \mathbf{x}_{\mathcal{G}_0}) \mathbf{c}^T \mathbf{P}(\mathbf{x}_{i, \mathcal{G}_k} - \mathbf{x}_{\mathcal{G}_0}) & \\ \mathbf{P}^T(\mathbf{x}_{i, \mathcal{G}_k} - \mathbf{x}_{\mathcal{G}_0}) & \\ = \frac{1}{2} \sum_{k \in \{\pm 1\}} \sum_i \mathcal{K}(\mathbf{x}_{i, \mathcal{G}_k} - \mathbf{x}_{\mathcal{G}_0}) \mathbf{P}^T(\mathbf{x}_{i, \mathcal{G}_k} - \mathbf{x}_{\mathcal{G}_0}) u_i & \\ \Rightarrow \mathbf{c} = \mathbf{M}^{-1}(\mathbf{x}_{\mathcal{G}_0}) \mathbf{b}(\mathbf{x}_{\mathcal{G}_0}) & \end{aligned}$$

where

$$\begin{aligned} \mathbf{M}(\mathbf{x}_{\mathcal{G}_0}) = & \\ \frac{1}{2} \sum_{k \in \{\pm 1\}} \sum_i \mathcal{K}(\mathbf{x}_{i, \mathcal{G}_k} - \mathbf{x}_{\mathcal{G}_0}) \mathbf{P}(\mathbf{x}_{i, \mathcal{G}_k} - \mathbf{x}_{\mathcal{G}_0}) \mathbf{P}^T(\mathbf{x}_{i, \mathcal{G}_k} - \mathbf{x}_{\mathcal{G}_0}) & \quad (26) \end{aligned}$$

and

$$\mathbf{b}(\mathbf{x}_{\mathcal{G}_0}) = \frac{1}{2} \sum_{k \in \{-1, +1\}} \sum_i \mathcal{K}(\mathbf{x}_{i, \mathcal{G}_k} - \mathbf{x}_{\mathcal{G}_0}) \mathbf{P}(\mathbf{x}_{i, \mathcal{G}_k} - \mathbf{x}_{\mathcal{G}_0}) u_i \quad (27)$$

Hence, with Equation 24, Equation 26, and Equation 27, we may approximate $u(\mathbf{z})$ with:

$$u(\mathbf{z}_{\mathcal{G}_0}) = \frac{1}{2} \sum_{k \in \{\pm 1\}} \sum_i \mathcal{K}(\mathbf{x}_{i, \mathcal{G}_k} - \mathbf{x}_{\mathcal{G}_0}) \mathbf{P}^T(\mathbf{z}_{\mathcal{G}_0} - \mathbf{x}_{\mathcal{G}_0}) \mathbf{M}^{-1} \mathbf{P}(\mathbf{x}_{i, \mathcal{G}_k} - \mathbf{x}_{\mathcal{G}_0}) u_i \quad (28)$$

With Equation 28 above, we can construct a nodal shape function for $\mathbf{x}_{i, \mathcal{G}_k}$ as:

$$\Phi_{i, \mathcal{G}_k}(\mathbf{z}_{\mathcal{G}_0}) = \mathcal{K}(\mathbf{x}_{i, \mathcal{G}_k} - \mathbf{x}_{\mathcal{G}_0}) \mathbf{P}^T(\mathbf{z}_{\mathcal{G}_0} - \mathbf{x}_{\mathcal{G}_0}) \mathbf{M}^{-1}(\mathbf{x}_{\mathcal{G}_0}) \mathbf{P}(\mathbf{x}_{i, \mathcal{G}_k} - \mathbf{x}_{\mathcal{G}_0}) \quad (29)$$

Thus, the approximation of u at $\mathbf{z}_{\mathcal{G}_0}$ can be expressed as:

$$u(\mathbf{z}_{\mathcal{G}_0}) = \frac{1}{2} \sum_{k \in \{\pm 1\}} \sum_i \Phi_{i, \mathcal{G}_k}(\mathbf{z}_{\mathcal{G}_0}) u_i, \quad (30)$$

where Φ_{i, \mathcal{G}_k} are the shape functions. If we choose the polynomial basis to consist of monomials in 3D, this formulation aligns with the original MLS-MPM approximation presented in prior work. However, note that our momentum matrix $\mathbf{M}(\mathbf{x}_{\mathcal{G}_0})$ cannot be simplified into a closed-form expression due to the dual-grid system. Consequently, we compute the momentum matrix for each particle independently at every timestep.

4 Implementation

In this section, we describe the implementation details of our CK-MPM scheme and outline optimizations to the computational pipeline.

4.1 General Pipeline

We adopt the state-of-the-art open-source GPU MPM framework proposed by Wang et al. [2020] as the foundation for our implementation. Specifically, we utilize the G2P2G algorithm and the Array-of-Structures-of-Arrays (AoSoA) data structure described in their work, incorporating our modified compact kernel and dual-grid system. One limitation of their implementation is that test-case parameters are hard-coded, making configuration adjustments labor-intensive. To address this, we follow the policy-based design pattern and extensively use C++ templates and ‘constexpr’ to encode material parameters and grid settings separately in each test file, improving flexibility and ease of use while maintaining runtime efficiency.

4.2 Dual-Grid Storage

The original grid data structure in Wang et al. [2020] stores information for each grid block (of size $4 \times 4 \times 4$ cells) in a contiguous memory segment. Within this block granularity, grid attributes are grouped in a *Structure-of-Arrays* (SoA) layout, enabling efficient coalesced read/write access to global GPU memory. We extend this scheme to a four-level index system, descending in the order of block index, grid index, attribute index, and cell index. In our dual-grid system, two grid blocks (from \mathcal{G}_+ and \mathcal{G}_-) share the same block index if the bottom-left cell of the block in \mathcal{G}_+ is offset by $\frac{1}{2}e^\alpha$ relative to the corresponding block in \mathcal{G}_- . By treating paired grid blocks as a single entity and introducing the grid index as an additional level, we efficiently manage data access within the dual-grid framework.

4.3 Particle Block

In the original implementation by Wang et al. [2020], particle blocks are offset by two cells from their corresponding grid blocks to satisfy the requirements of the G2P2G algorithm under a proper CFL constraint. In our dual-grid scheme, we modify this relationship to account for the additional grid. Without loss of generality, we designate grid blocks from \mathcal{G}_- as the reference blocks for defining the new particle blocks. This ensures compatibility with the dual-grid configuration.

4.4 Kernel Optimization

The G2P2G algorithm requires grid data to be loaded into shared memory. In our dual-grid scheme, this results in twice the shared memory usage compared to the original implementation, which can limit the number of parallel CUDA blocks running concurrently due to the finite shared memory available per Streaming Multiprocessor (SM). To address this, we optimize the memory usage by reducing the number of grid cells loaded into shared memory.

As illustrated in Figure 3, under the CFL restriction, particles in a particle block will never reach the top, right, or back layers of their corresponding grid blocks in \mathcal{G}_+ . Exploiting this observation, we reduce the number of cells loaded from $2 \times 8^3 = 1024$ to $8^3 + 7^3 = 855$, achieving a 16.5% reduction in shared memory usage per CUDA block. For each cell, 3 floats are required for velocity in the G2P process and 4 floats for mass and momentum in the P2G process. Consequently, the shared memory usage decreases from $1024 \cdot 7 \cdot 4 = 28,672$ bytes to $855 \cdot 7 \cdot 4 = 23,940$ bytes.

On an NVIDIA RTX 3090 GPU with CUDA compute capability 8.6, the maximum available shared memory per SM is 100 KB. This reduction increases the maximum number of concurrent CUDA blocks per SM from 3 to 4, resulting in a 33.3% improvement in concurrency. This optimization significantly enhances the performance of our dual-grid implementation.

5 Experiment

In the following subsections, we first validate our CK-MPM by demonstrating that it successfully passes unit tests commonly used in computational mechanics (subsection 5.1). Next, we compare the performance and behavior of our CK-MPM against the state-of-the-art open-source GPU MPM framework [Wang et al. 2020] (subsection 5.2). Finally, we showcase the robustness and versatility of our method through stress tests involving large-scale scenes and complex geometries (subsection 5.3).

Except for the stress tests, all experiments are conducted on a machine equipped with an Intel Core i9-12900KF CPU and an NVIDIA RTX 3090 GPU. The system runs CUDA 12.4 with NVIDIA driver version 550.54. For code compilation, we use gcc/g++ 12.3 with the C++20 standard enforced. All source code will be made publicly available.

5.1 Unit tests

In this subsection, we evaluate the conservation properties of our CK-MPM method using the fixed-rotated hyperelasticity model [Stomakhin et al. 2012] for all test cases.

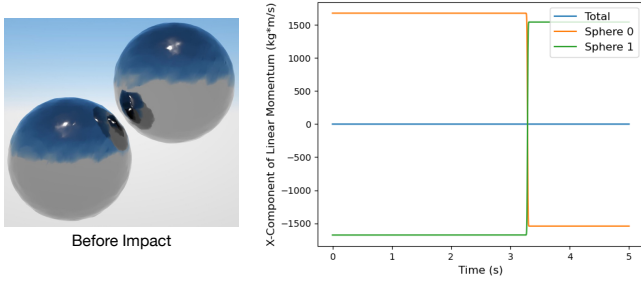


Fig. 4. **Linear momentum conservation.** The evolution of the x -component of the total linear momentum (blue) and the linear momentum of two spheres (green and orange).

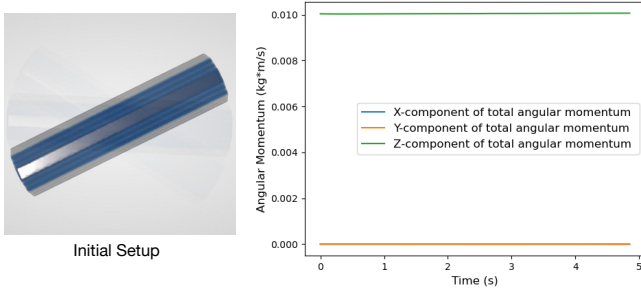


Fig. 5. **Angular momentum conservation.** Evolution of x -, y -, z -component of the total angular momentum of a rotating bar simulation; all components are accurately preserved over time.

Conservation of linear momentum. To verify the conservation of linear momentum, we simulate a simple test case involving two colliding spheres. Each sphere has a radius of $\frac{10}{256}$ m and is discretized with 8 particles per cell, using a cell spacing of $dx = \frac{1}{256}$ m. This results in 33,552 particles per sphere. The material parameters are set as $E = 10^6$ Pa, $\nu = 0.4$, and $\rho = 10^3$ kg/m³. The spheres are initially located at $(\frac{32}{256}, \frac{32}{256}, \frac{32}{256})$ m and $(\frac{128}{256}, \frac{128}{256}, \frac{128}{256})$ m, with initial velocities of $(0.05, 0.05, 0.05)$ m/s and $(-0.05, -0.05, -0.05)$ m/s, respectively. Thus, the norm of the total linear momentum for each sphere is approximately 2905.69 kg·m/s, while the total initial linear momentum of the system is zero.

We simulate the system for 5 seconds and measure the ratio of the norm of the total linear momentum of the system to the initial linear momentum of one sphere. To avoid numerical instabilities, we use double-precision floating-point numbers for kernel computations and collect particle velocities instead of momentum, as the particle masses are small and fixed. As shown in Figure 4, the x -component of the total linear momentum remains nearly zero while the x -component of the linear momentum of two spheres interchanges after collision, demonstrating the near-negligible error and the strong capability of our method to conserve total linear momentum.

Conservation of angular momentum. Next, we evaluate the conservation of angular momentum using a rotating rod test case. The rod is initialized as a cylinder with a radius of $\frac{5}{256}$ m and a length

Table 2. We use the MLS MPM in both Wang et al. [2020] and our implementation. All examples are simulated for 100 frames with 48 frames per second and a grid resolution of $(256, 256, 256)$.

Example	Wang et al. [2020]	Ours	Speedup
Two Dragons Falling	1.28	0.64	2×
Fluid Dam Break	6.12	2.61	2.34×
Droplet Impact	6.59	2.50	2.64×
Sand Armadillos	1.07	0.54	1.98×

of $\frac{40}{256}$ m, with its central axis aligned with the z -axis. The material parameters are set as $E = 10^6$ Pa, $\nu = 0.4$, and $\rho = 10^3$ kg/m³. The center of the cylinder is positioned at $(\frac{128}{256}, \frac{128}{256}, \frac{128}{256})$ m. For each particle at a z -axis distance Δr_p from the center of the cylinder, we assign velocities of $(\pm \frac{256\Delta r_p}{20}, 0, 0)$ m/s on opposite sides of the cylinder, ensuring that the endpoints have velocities of $(\pm 1, 0, 0)$ m/s.

We measure the evolution of the x -, y -, and z -components of the total angular momentum over 5 seconds. As shown in Figure 5, these components remain nearly constant throughout the simulation. To reduce numerical errors, we compute the angular momentum as $\sum_p \mathbf{x}_p \times \mathbf{v}_p$, avoiding multiplication with small particle masses. These results confirm that our method effectively conserves total angular momentum during the simulation.

5.2 Comparisons

In this subsection, we present several test cases to evaluate the performance improvements and behavioral differences between our CK-MPM and the traditional quadratic B-spline MPM.

5.2.1 Speedup. As discussed in section 4, our method incorporates an adapted version of the G2P2G algorithm [Wang et al. 2020]. Since G2P2G represents the most computationally intensive operation in each substep, we begin by highlighting the speedup achieved in G2P2G computations using our CK-MPM approach.

We compare four of our test cases against the implementation by Wang et al. [2020]. For both methods, we measure and calculate the average computation time of the G2P2G kernel. The experiments are carefully designed to ensure comparable behavior across the first 100 frames, enabling a consistent and fair performance evaluation.

Two Dragons Falling. We initialize two dragon models with zero initial velocity, discretized into a total of 775,196 particles. The dragons are simulated using a fixed-corotated hyperelasticity model with Young’s modulus $E = 6 \times 10^5$ Pa and Poisson’s ratio $\nu = 0.4$. The gravity is set to -4 m/s². As shown in Figure 6, the simulation captures the realistic deformation and collision dynamics as the dragons fall and interact.

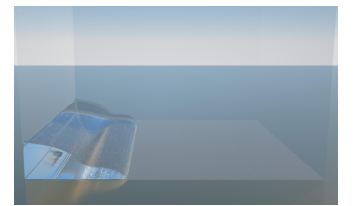


Fig. 7. **Fluid Dam Break.**

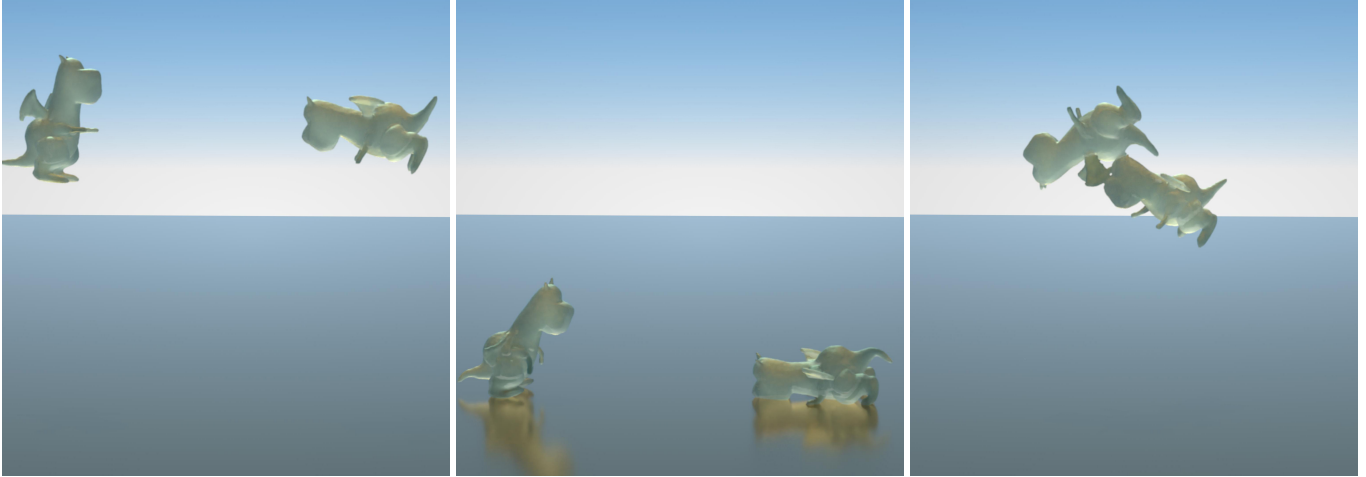


Fig. 6. Two Dragons Falling.

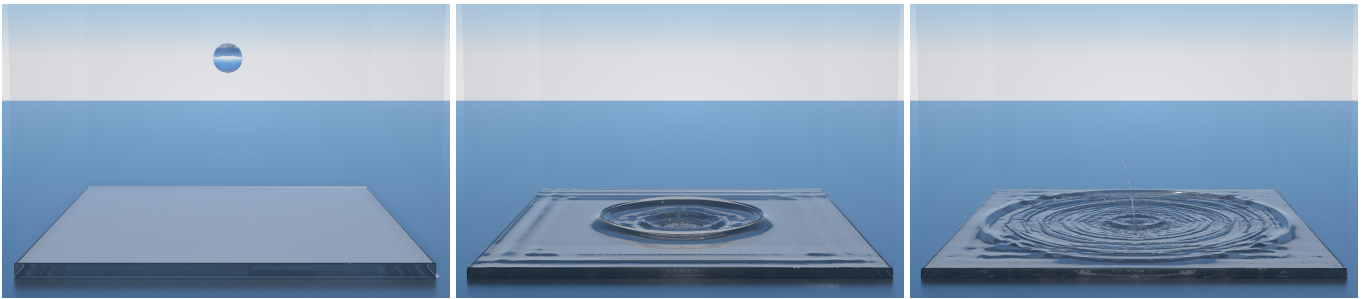


Fig. 8. Droplet Impact.

Fluid Dam Break. A total of 3,776,000 particles are initialized with a uniform distribution in a cuboid to simulate a single dam break. The fluid is modeled using the equation of state formulation [Monaghan 1994; Tampubolon et al. 2017], or the J -based fluid model, with parameters: $B = 10Pa$, $\gamma = 7.15$, and viscosity $\mu = 0.1$. Gravity is set to -2 m/s^2 . As shown in Figure 7, the simulation captures the realistic flow dynamics as the fluid rushes outward after the dam break.

Droplet Impact. A spherical fluid droplet is initialized with zero velocity above a uniformly sampled fluid cuboid in a tank, with a total of 3,658,768 particles. The droplet and fluid surface share the same material parameters as the dam break example. As shown in Figure 8, the droplet impacts the surface, creating waves that propagate outward and eventually generate tiny splashes of water.

Sand Armadillos. Two armadillo models are initialized with opposing initial velocities of $(0, 0, -0.5)$ and $(0, 0, 0.5)$ m/s, respectively, and discretized into 511,902 particles. The simulation uses the Drucker-Prager elastoplasticity model with parameters $E = 10^4$ Pa and $\nu = 0.4$. Gravity is set to -2 m/s^2 . As shown in Figure 11, the simulation captures the collapse and dispersion of the armadillos with fine granularity, demonstrating realistic sand behavior.

In Table 2, we observe that our compact kernel can achieve a more than $2\times$ speedup in the most computationally intensive step of the MPM pipeline, primarily by reducing the number of atomic operations.

5.2.2 Behavior Analysis. We compare the behavioral differences between MPM simulations using our compact kernel and the standard quadratic kernel.

Fracture Behavior. Due to the smaller kernel radius, MPM simulations using our compact kernel are more prone to generating fractures upon collision. To illustrate this behavioral difference, we present two test cases.

The first test case, *Pumpkin Smash*, involves two pumpkin models, with one resting on the ground and the other falling from above. The pumpkins are simulated using the Non-Associated Cam Clay (NACC) [Wolper et al. 2019] model with parameters $E = 2000Pa$, $\nu = 0.39$, $\alpha_0 = -0.04$, $\beta = 2$, $\xi = 3$, and $M = 2.36$. The initial drop height of the falling pumpkin is set to $\frac{100}{128}m$, with a grid resolution of $(256, 256, 256)$, $\Delta x = \frac{1}{128}m$, and gravity $g = -2\text{ m/s}^2$. As shown in Figure 9, the pumpkins simulated with the compact kernel produce significant fractures, while those simulated with the quadratic kernel exhibit elastic behavior, bouncing back after a brief period of compression.

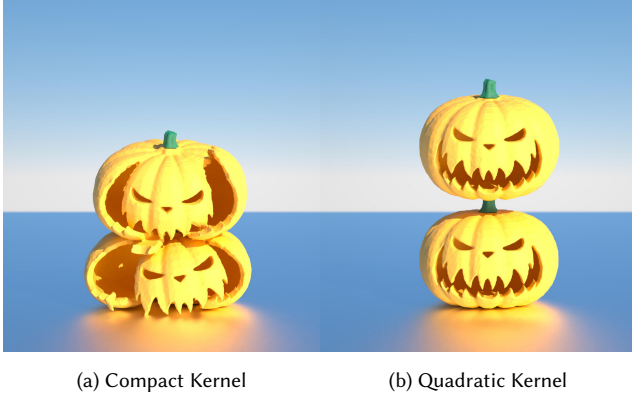


Fig. 9. Pumpkin Smash.

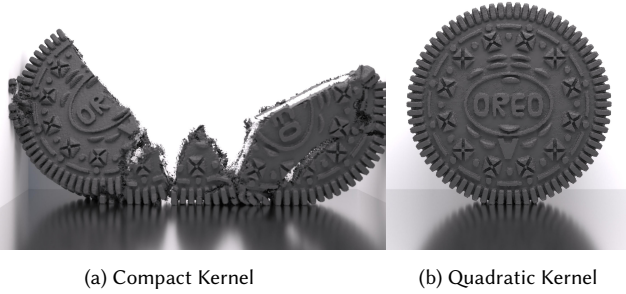


Fig. 10. Oreo Drop.

In the second test case, *Oreo Drop*, we simulate an Oreo-like structure consisting of a heart and crust falling to the ground. Both parts are modeled using the NACC model with parameters $E = 2 \times 10^4 \text{ Pa}$, $\nu = 0.4$, $\alpha_0 = -0.01$, $\beta = 0.1$, $\xi = 0.8$, and $M = 2.36$. The initial drop height of the Oreo is set to $\frac{16}{256}$, and the simulation is conducted with gravity $g = -9.8 \text{ m/s}^2$. As shown in Figure 10, the Oreo simulated with the compact kernel fractures and falls apart, while the one simulated with the quadratic kernel retains its original shape. Additionally, the Oreo demonstrates more brittle fractures compared to the pumpkin due to its complex geometry and structural subtleties.

These results highlight the different fracture behaviors induced by the compact kernel, particularly in scenarios involving collisions and complex geometries. Notably, our method achieves realistic fracture animations without relying on a phase-field model, which explicitly tracks fracture surfaces and softens materials to facilitate crack generation, as demonstrated in [Wolper et al. 2020, 2019]. This capability underscores the efficiency and simplicity of our approach in capturing fracture dynamics without the additional computational overhead associated with phase-field methods.

5.3 Stress tests

To evaluate the stability and robustness of our compact-kernel MPM under extreme conditions, we conducted a series of stress tests. A

summary of the results is presented in Table 3. The stress tests are categorized into two primary types: (1) large-scale simulations involving high-resolution grids and a large number of particles, and (2) simulations with extreme material parameter settings, designed to push the limits of stability and performance. All simulations were performed on an Intel Xeon w7-3455 CPU and a single NVIDIA RTX 6000 Ada GPU, using CUDA 12.4 and CUDA driver version 550.54.14. For the C++ backend, we employed gcc/g++ 12.3 as the compiler. Below, we provide a concise summary of each test case, highlighting the challenges posed and the performance of our method.

Fluid Flush with Two Longs. We simulate a large-scale scene with grid resolutions of (1024, 512) and a grid spacing of $\Delta x = \frac{1}{512} \text{ m}$. The simulation features a cuboid of water, uniformly sampled with 76,185,600 particles, and two longs placed near the center of the scene, discretized with 8,219,227 particles. The fluid is modeled using the J -based fluid model with $B = 10 \text{ Pa}$, $\gamma = 7.15$, and viscosity $\mu = 0.1$. The longs are simulated using the Fixed Corotated hyperelasticity model with Young’s modulus $E = 10^6 \text{ Pa}$ and Poisson’s ratio $\nu = 0.3$. As shown in Figure 12, the simulation demonstrates detailed interactions between water and the longs, with clear splashing and turbulence effects.

Sand Castle Crashing. This test involves a sandcastle discretized with 45,925,181 particles on a grid with resolution (2048, 1024, 1024) and a grid spacing of $\Delta x = \frac{1}{512} \text{ m}$. The sand is modeled using the Non-Associative Cam Clay (NACC) model [Wolper et al. 2019] with parameters $E = 10^4 \text{ Pa}$, $\nu = 0.4$, $\alpha_0 = -0.006$, $\beta = 0.3$, $\xi = 0.5$, and $M = 1.85$. Additionally, a cannonball, discretized with 33,552 particles, is initialized with an initial velocity of (10, 0, 0) m/s and simulated using the Fixed Corotated model with $E = 10^7 \text{ Pa}$ and $\nu = 0.2$. To prevent premature collapse of the sandcastle under self-weight and preserve detailed features, we set gravity to $g = -0.1 \text{ m/s}^2$. Figure 1 captures the dramatic destruction of the sandcastle as the cannonball collides, preserving intricate details of the collapsing structure.

Bullet Impact on Tungsten. This test explores the stability of our method under extreme impact conditions. The setup includes a lead bullet with an initial velocity of (300, 0, 0) m/s striking a tungsten cube with a side length of 0.1 m. The lead bullet is simulated with real-world material parameters: gravity $g = 9.8 \text{ m/s}^2$, Young’s modulus $E = 1.5 \times 10^{10} \text{ Pa}$, and Poisson’s ratio $\nu = 0.435$. The tungsten cube is modeled using the Fixed Corotated hyperelasticity model with $E = 4.5 \times 10^{11} \text{ Pa}$ and $\nu = 0.27$. As illustrated in Figure 13, the sequence shows the bullet’s progression before, during, and after impact, with visible deformation and subtle vibration modes on the tungsten cube.

6 Conclusion

In this work, we introduced CK-MPM, a compact-kernel material point method, featuring a novel C^2 -continuous compact kernel integrated into a staggered dual-grid framework. Our approach ensures that each particle is exclusively associated with the grid nodes of the cell it occupies per grid, enabling a significant reduction in P2G2P costs—nearly 50% compared to quadratic B-spline MPM. CK-MPM is fully compatible with existing PIC, Affine PIC, and MLS-MPM

Table 3. Simulation statistics of our stress tests.

Example	Average sec/frame	Frame Δt (s)	Maximum Δt (s)	Particle count	Δx (m)	Grid resolution
Fluid Flush with Two Longs	16.403	$\frac{1}{48}$	4.6×10^{-5}	84,404,827	$\frac{1}{512}$	(1024, 512, 512)
Bullet Impact on Tungsten	4.847	$\frac{1}{10^4}$	9.03×10^{-8}	8,655,462	$\frac{1}{1024}$	(1024, 1024, 1024)
Sand Castle Crashing	7.37	$\frac{1}{480}$	9.26×10^{-6}	45,958,733	$\frac{1}{512}$	(2048, 1024, 1024)

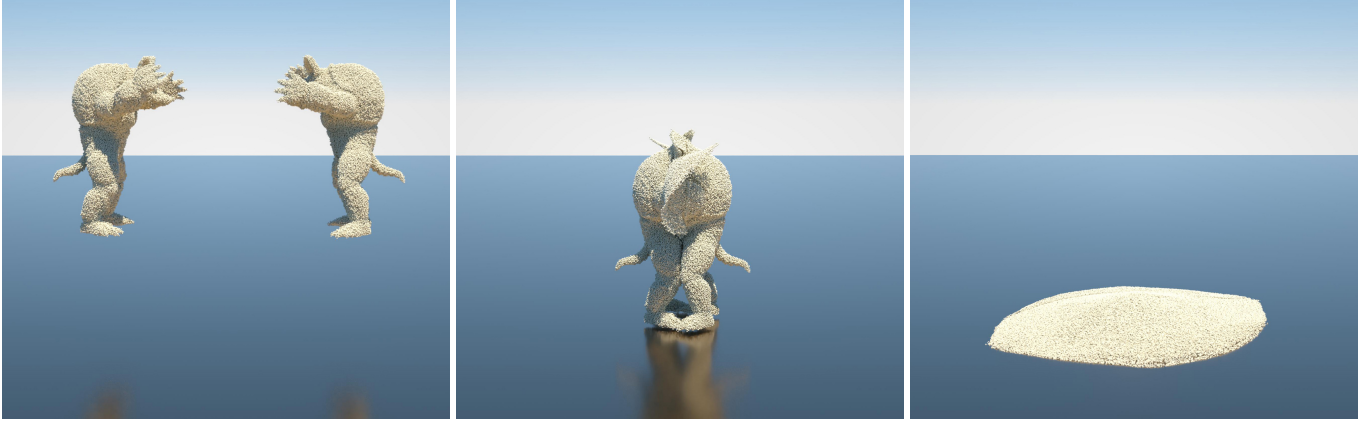


Fig. 11. Sand Armadillos.

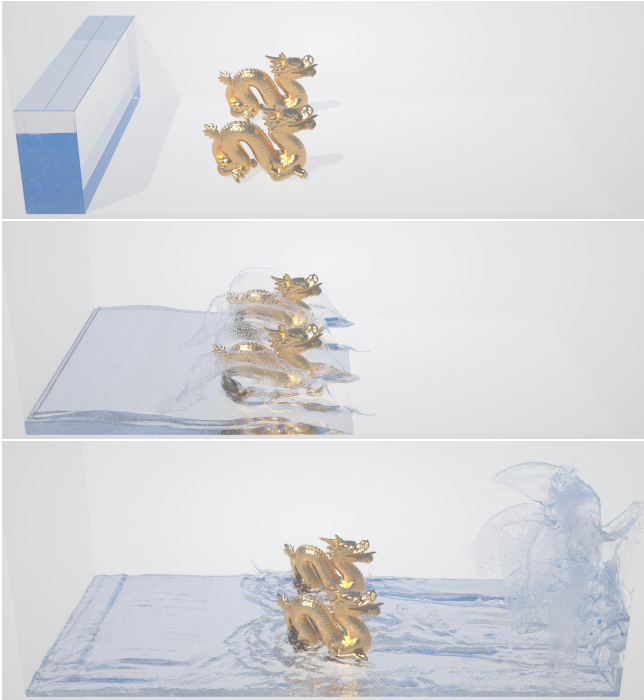


Fig. 12. Fluid Flush with Two Longs.

schemes, preserving critical physical properties such as linear and angular momentum. Through extensive testing, we demonstrated

the robustness and efficiency of our method across a wide range of large-scale simulations, including scenarios involving extreme stiffness, high-speed impacts, and other challenging setups. By combining compact support, high-order continuity, and compatibility with established MPM schemes, CK-MPM represents a step forward in efficiency for MPM simulations. We believe our approach lays a strong foundation for further advancements in physics-based simulation, empowering applications in engineering, computer graphics, and beyond.

Limitations & Future Works. While the staggered grid framework in our method adds complexity to the implementation, it opens avenues for meaningful future research. For instance, further optimizing memory layouts on multi-GPU or multinode computing environments could unlock additional speedups, enabling even more scalable simulations. Another intriguing direction lies in the trade-off between efficiency and accuracy in the CUDA trigonometric functions. The intrinsic CUDA functions `__sinf` and `__cosf`, though faster, lack the precision required to accurately preserve momentum. To ensure accuracy, we currently rely on the slower `sin` and `cos` functions. Future advancements in CUDA's implementation of faster and more precise trigonometric functions would directly enhance the performance of our method. Our compact kernel, with its small support size, has a tendency to facilitate material fractures. This can be advantageous for fracture simulations but presents challenges for scenarios requiring fracture-free large deformations. In such cases, increasing the particle density per cell could mitigate unwanted fractures. Additionally, we believe that our compact kernel holds potential for implicit MPM formulations, where it could similarly improve stability and efficiency. Finally, our method preserves the

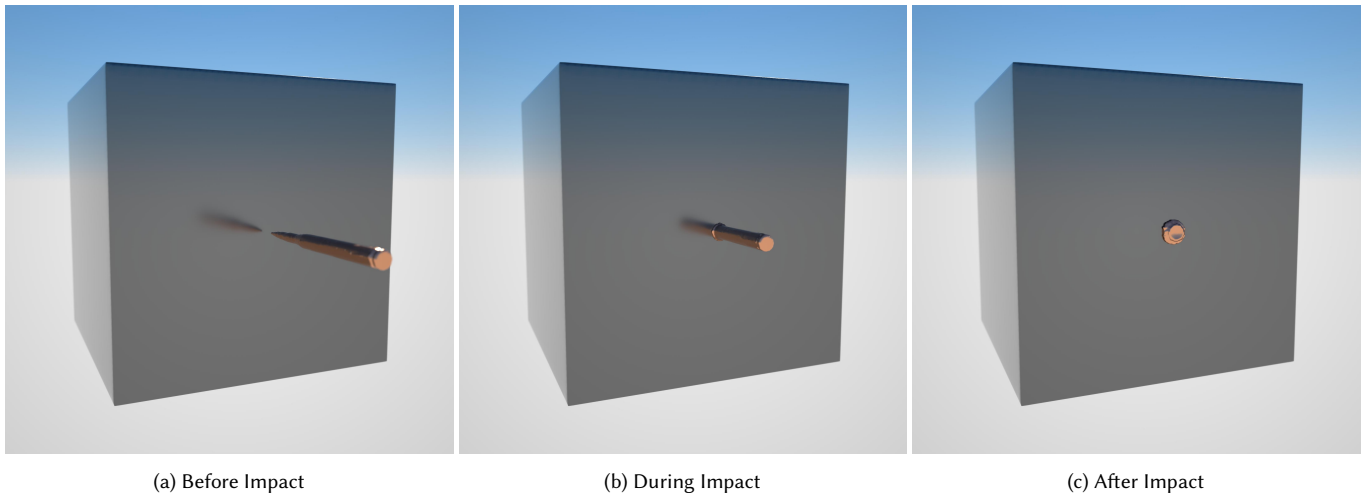


Fig. 13. Bullet Impact on Tungsten.

differentiability of MPM simulations, making it highly suitable for solving inverse problems, such as those explored in [Huang et al. \[2024\]](#); [Zhang et al. \[2025\]](#). We envision that the combination of high efficiency and differentiability could significantly advance applications in 3D reconstruction, data-driven design, etc.

References

- Scott G Bardenhagen, Edward M Kober, et al. 2004. The generalized interpolation material point method. *Computer Modeling in Engineering and Sciences* 5, 6 (2004), 477–496.
- Yadi Cao, Yunuo Chen, Minchen Li, Yin Yang, Xinxin Zhang, Mridul Aanjaneya, and Chenfanfu Jiang. 2022. An efficient b-spline lagrangian/eulerian method for compressible flow, shock waves, and fracturing solids. *ACM Transactions on Graphics (TOG)* 41, 5 (2022), 1–13.
- Peter Yichen Chen, Maytee Chantharayukhonthorn, Yonghao Yue, Eitan Grinspun, and Ken Kamrin. 2021. Hybrid discrete-continuum modeling of shear localization in granular media. *Journal of the Mechanics and Physics of Solids* 153 (2021), 104404.
- Alban De Vaucorbeil, Vinh Phu Nguyen, Sina Sinaie, and Jian Ying Wu. 2020. Material point method after 25 years: theory, implementation, and applications. *Advances in applied mechanics* 53 (2020), 185–398.
- Mengyuan Ding, Xuchen Han, Stephanie Wang, Theodore F Gast, and Joseph M Teran. 2019. A thermomechanical material point method for baking and cooking. *ACM Transactions on Graphics (TOG)* 38, 6 (2019), 1–14.
- Yu Fang, Minchen Li, Ming Gao, and Chenfanfu Jiang. 2019. Silly rubber: an implicit material point method for simulating non-equilibrated viscoelastic and elastoplastic solids. *ACM Transactions on Graphics (TOG)* 38, 4 (2019), 1–13.
- Yu Fang, Ziyin Qu, Minchen Li, Xinxin Zhang, Yixin Zhu, Mridul Aanjaneya, and Chenfanfu Jiang. 2020. IQ-MPM: an interface quadrature material point method for non-sticky strongly two-way coupled nonlinear solids and fluids. *ACM Transactions on Graphics (TOG)* 39, 4 (2020), 51–1.
- Yun Fei, Christopher Batty, Eitan Grinspun, and Changxi Zheng. 2018. A multi-scale model for simulating liquid-fabric interactions. *ACM Transactions on Graphics (TOG)* 37, 4 (2018), 1–16.
- Yun Fei, Christopher Batty, Eitan Grinspun, and Changxi Zheng. 2019. A multi-scale model for coupling strands with shear-dependent liquid. *ACM Transactions on Graphics (TOG)* 38, 6 (2019), 1–20.
- Yun Fei, Henrique Teles Maia, Christopher Batty, Changxi Zheng, and Eitan Grinspun. 2017. A multi-scale model for simulating liquid-hair interactions. *ACM Transactions on Graphics (TOG)* 36, 4 (2017), 1–17.
- Johan Gaume, T Gast, Joseph Teran, Alec van Herwijnen, and Chenfanfu Jiang. 2018. Dynamic anticrack propagation in snow. *Nature communications* 9, 1 (2018), 3047.
- Qi Guo, Xuchen Han, Chuyuan Fu, Theodore Gast, Rasmus Tamstorf, and Joseph Teran. 2018. A material point method for thin shells with frictional contact. *ACM Transactions on Graphics (TOG)* 37, 4 (2018), 1–15.
- Xuchen Han, Theodore F Gast, Qi Guo, Stephanie Wang, Chenfanfu Jiang, and Joseph Teran. 2019. A hybrid material point method for frictional contact with diverse materials. *Proceedings of the ACM on Computer Graphics and Interactive Techniques* 2, 2 (2019), 1–24.
- Francis H Harlow. 1962. *The particle-in-cell method for numerical solution of problems in fluid dynamics*. Technical Report. Los Alamos National Lab.(LANL), Los Alamos, NM (United States).
- Yuanming Hu, Yu Fang, Ziheng Ge, Ziyin Qu, Yixin Zhu, Andre Pradhana, and Chenfanfu Jiang. 2018. A moving least squares material point method with displacement discontinuity and two-way rigid body coupling. *ACM Transactions on Graphics (TOG)* 37, 4 (2018), 1–14.
- Tianyu Huang, Haoze Zhang, Yihan Zeng, Zhilu Zhang, Hui Li, Wangmeng Zuo, and Rynson WH Lau. 2024. Dreamphysics: Learning physical properties of dynamic 3d gaussians with video diffusion priors. *arXiv preprint arXiv:2406.01476* (2024).
- Chenfanfu Jiang, Theodore Gast, and Joseph Teran. 2017. Anisotropic elastoplasticity for cloth, knit and hair frictional contact. *ACM Transactions on Graphics (TOG)* 36, 4 (2017), 1–14.
- Chenfanfu Jiang, Craig Schroeder, Andrew Selle, Joseph Teran, and Alexey Stomakhin. 2015. The affine particle-in-cell method. *ACM Transactions on Graphics (TOG)* 34, 4 (2015), 1–10.
- Chenfanfu Jiang, Craig Schroeder, Joseph Teran, Alexey Stomakhin, and Andrew Selle. 2016. The material point method for simulating continuum materials. In *Acem siggraph 2016 courses*. 1–52.
- Victoria Kala, Jingyu Chen, David Hyde, Alexey Stomakhin, and Joseph Teran. 2024. A Thermomechanical Hybrid Incompressible Material Point Method. *arXiv preprint arXiv:2408.07276* (2024).
- Gergely Klár, Theodore Gast, Andre Pradhana, Chuyuan Fu, Craig Schroeder, Chenfanfu Jiang, and Joseph Teran. 2016. Drucker-prager elastoplasticity for sand animation. *ACM Transactions on Graphics (TOG)* 35, 4 (2016), 1–12.
- Yong Liang, Xiong Zhang, and Yan Liu. 2019. An efficient staggered grid material point method. *Computer Methods in Applied Mechanics and Engineering* 352 (2019), 85–109.
- Joe J Monaghan. 1994. Simulating free surface flows with SPH. *Journal of computational physics* 110, 2 (1994), 399–406.
- Georgios Moutsanidis, Christopher C Long, and Yuri Bazilevs. 2020. IGA-MPM: the isogeometric material point method. *Computer Methods in Applied Mechanics and Engineering* 372 (2020), 113346.
- Alireza Sadeghirad, Rebecca M Brannon, and Jeff Burghardt. 2011. A convected particle domain interpolation technique to extend applicability of the material point method for problems involving massive deformations. *International Journal for numerical methods in Engineering* 86, 12 (2011), 1435–1456.
- Michael Steffen, Robert M Kirby, and Martin Berzins. 2008. Analysis and reduction of quadrature errors in the material point method (MPM). *International journal for numerical methods in engineering* 76, 6 (2008), 922–948.
- Alexey Stomakhin, Russell Howes, Craig A Schroeder, and Joseph M Teran. 2012. Energetically Consistent Invertible Elasticity. In *Symposium on Computer Animation*, Vol. 1.
- Alexey Stomakhin, Craig Schroeder, Lawrence Chai, Joseph Teran, and Andrew Selle. 2013. A material point method for snow simulation. *ACM Transactions on Graphics (TOG)* 32, 4 (2013), 1–10.

- Alexey Stomakhin, Craig Schroeder, Chenfanfu Jiang, Lawrence Chai, Joseph Teran, and Andrew Selle. 2014. Augmented MPM for phase-change and varied materials. *ACM Transactions on Graphics (TOG)* 33, 4 (2014), 1–11.
- Haozhe Su, Tao Xue, Chengguizi Han, Chenfanfu Jiang, and Mridul Aanjaneya. 2021. A unified second-order accurate in time MPM formulation for simulating viscoelastic liquids with phase change. *ACM Transactions on Graphics (TOG)* 40, 4 (2021), 1–18.
- Deborah Sulsky, Shi-Jian Zhou, and Howard L Schreyer. 1995. Application of a particle-in-cell method to solid mechanics. *Computer physics communications* 87, 1-2 (1995), 236–252.
- Andre Pradhana Tampubolon, Theodore Gast, Gergely Klár, Chuyuan Fu, Joseph Teran, Chenfanfu Jiang, and Ken Museth. 2017. Multi-species simulation of porous sand and water mixtures. *ACM Transactions on Graphics (TOG)* 36, 4 (2017), 1–11.
- Xinlei Wang, Yuxing Qiu, Stuart R Slattery, Yu Fang, Minchen Li, Song-Chun Zhu, Yixin Zhu, Min Tang, Dinesh Manocha, and Chenfanfu Jiang. 2020. A massively parallel and scalable multi-GPU material point method. *ACM Transactions on Graphics (TOG)* 39, 4 (2020), 30–1.
- Peter Wilson, Roland Wüchner, and Dilum Fernando. 2021. Distillation of the material point method cell crossing error leading to a novel quadrature-based C 0 remedy. *Internat. J. Numer. Methods Engrg.* 122, 6 (2021), 1513–1537.
- Joshuah Wolper, Yunuo Chen, Minchen Li, Yu Fang, Ziyin Qu, Jiecong Lu, Meggie Cheng, and Chenfanfu Jiang. 2020. Anisompm: Animating anisotropic damage mechanics: Supplemental document. *ACM Trans. Graph* 39, 4 (2020).
- Joshuah Wolper, Yu Fang, Minchen Li, Jiecong Lu, Ming Gao, and Chenfanfu Jiang. 2019. CD-MPM: continuum damage material point methods for dynamic fracture animation. *ACM Transactions on Graphics (TOG)* 38, 4 (2019), 1–15.
- Yonghao Yue, Breannan Smith, Peter Yichen Chen, Maytee Chantharayukhonthorn, Ken Kamrin, and Eitan Grinspun. 2018. Hybrid grains: Adaptive coupling of discrete and continuum simulations of granular media. *ACM Transactions on Graphics (TOG)* 37, 6 (2018), 1–19.
- Duan Z Zhang, Xia Ma, and Paul T Giguere. 2011. Material point method enhanced by modified gradient of shape function. *J. Comput. Phys.* 230, 16 (2011), 6379–6398.
- Tianyuan Zhang, Hong-Xing Yu, Rundi Wu, Brandon Y Feng, Changxi Zheng, Noah Snavely, Jiajun Wu, and William T Freeman. 2025. Physdreamer: Physics-based interaction with 3d objects via video generation. In *European Conference on Computer Vision*. Springer, 388–406.
- Yidong Zhao, Jinhun Choo, Yupeng Jiang, and Liuchi Li. 2023. Coupled material point and level set methods for simulating soils interacting with rigid objects with complex geometry. *Computers and Geotechnics* 163 (2023), 105708.
- Zeshun Zong, Xuan Li, Minchen Li, Maurizio M Chiaramonte, Wojciech Matusik, Eitan Grinspun, Kevin Carlberg, Chenfanfu Jiang, and Peter Yichen Chen. 2023. Neural stress fields for reduced-order elastoplasticity and fracture. In *SIGGRAPH Asia 2023 Conference Papers*. 1–11.

A Proof of Linear Momentum Conservation with PIC

Traditional PIC pipeline preserves linear momentum in P2G, grid update, and G2P steps. We show a similar result in our new dual grid system.

THEOREM A.1 (CONSERVATION OF LINEAR MOMENTUM WITH PIC). *The total linear momentum is preserved in P2G, grid update, and P2G steps in PIC scheme by defining the total linear momentum of the grid as:*

$$\mathbf{p}_{\text{grid total}, t_n}^\alpha := \frac{1}{2} \sum_{k \in \{-1, +1\}} \mathbf{P}_{\mathcal{G}_k, t_n}^\alpha = \frac{1}{2} \sum_{k \in \{\pm 1\}} \sum_i m_{i, \mathcal{G}_k, t_n} \mathbf{v}_{i, \mathcal{G}_k, t_n}^\alpha \quad (31)$$

PROOF. Let's assume that the current time step is t_n . In P2G step, the total linear momentum of particle is $\sum_p m_p \mathbf{v}_{p, \mathcal{G}_0, t_n}^\alpha$. With the

particle-to-grid transfer for momentum (Equation 15), we note that:

$$\begin{aligned} & \sum_p m_p \mathbf{v}_{p, \mathcal{G}_0, t_n}^\alpha \\ &= \sum_p m_p \mathbf{v}_{p, \mathcal{G}_0, t_n}^\alpha \left(\frac{1}{2} \sum_{k \in \{\pm 1\}} \sum_i w_{i, p, \mathcal{G}_k, t_n} \right) \\ &= \frac{1}{2} \sum_{k \in \{-1, +1\}} \sum_i \sum_p w_{i, p, \mathcal{G}_k, t_n} m_p \mathbf{v}_{p, t_n}^\alpha \\ &= \frac{1}{2} \sum_{k \in \{\pm 1\}} \sum_i m_{i, \mathcal{G}_k, t_n} \mathbf{v}_{i, \mathcal{G}_k, t_n}^\alpha \end{aligned}$$

For grid update, we have:

$$\begin{aligned} & \frac{1}{2} \sum_{k \in \{\pm 1\}} \sum_i m_{i, \mathcal{G}_k, t_n} \tilde{\mathbf{v}}_{i, \mathcal{G}_k, t_n}^\alpha \\ &= \frac{1}{2} \sum_{k \in \{\pm 1\}} \sum_i \left(m_{i, \mathcal{G}_k, t_n} \mathbf{v}_{i, \mathcal{G}_k, t_n}^\alpha + \Delta t \mathbf{f}_{i, \mathcal{G}_k, t_n}^\alpha \right) \\ &= \frac{1}{2} \sum_{k \in \{\pm 1\}} \sum_i m_{i, \mathcal{G}_k, t_n} \mathbf{v}_{i, \mathcal{G}_k, t_n}^\alpha \\ & \quad + \frac{\Delta t}{2} \sum_{k \in \{\pm 1\}} \sum_i \sum_p V_p(\mathbf{P}_{p, \mathcal{G}_0, t_n})^\alpha (\mathbf{F}_{p, \mathcal{G}_0, t_n})^\beta (\nabla w_{i, p, \mathcal{G}_k, t_n})^\nu \\ &= \frac{1}{2} \sum_{k \in \{\pm 1\}} \sum_i m_{i, \mathcal{G}_k, t_n} \mathbf{v}_{i, \mathcal{G}_k, t_n}^\alpha \\ & \quad + \Delta t \sum_p V_p(\mathbf{P}_{p, \mathcal{G}_0, t_n})^\alpha (\mathbf{F}_{p, \mathcal{G}_0, t_n})^\beta \left(\frac{1}{2} \sum_{k \in \{\pm 1\}} \sum_i (\nabla w_{i, p, \mathcal{G}_k, t_n})^\nu \right) \\ &= \frac{1}{2} \sum_{k \in \{\pm 1\}} \sum_i m_{i, \mathcal{G}_k, t_n} \mathbf{v}_{i, \mathcal{G}_k, t_n}^\alpha \end{aligned}$$

Finally, with grid-to-particle equation (Equation 19), we have:

$$\begin{aligned} & \frac{1}{2} \sum_{k \in \{\pm 1\}} \sum_i m_{i, \mathcal{G}_k, t_n} \tilde{\mathbf{v}}_{i, \mathcal{G}_k, t_n}^\alpha \\ &= \frac{1}{2} \sum_{k \in \{\pm 1\}} \sum_i m_{i, \mathcal{G}_k, t_n} \tilde{\mathbf{v}}_{i, \mathcal{G}_k, t_n}^\alpha \left(\sum_p w_{i, p, \mathcal{G}_k, t_n} \right) \\ &= \frac{1}{2} \sum_{k \in \{\pm 1\}} \sum_i \sum_p m_{i, \mathcal{G}_k, t_n} w_{i, p, \mathcal{G}_k, t_n} \tilde{\mathbf{v}}_{i, \mathcal{G}_k, t_n}^\alpha \\ &= \sum_p \left(\frac{1}{2} \sum_{k \in \{\pm 1\}} \sum_i m_{i, \mathcal{G}_k, t_n} w_{i, p, \mathcal{G}_k, t_n} \tilde{\mathbf{v}}_{i, \mathcal{G}_k, t_n}^\alpha \right) \\ &= \sum_p m_p \mathbf{v}_{p, t_n}^\alpha \end{aligned}$$

□

B Proof of Momentum Conservation with APIC

THEOREM B.1 (CONSERVATION OF LINEAR MOMENTUM WITH APIC).

PROOF. Note that there is no difference in the grid evolution and grid-to-particle transfer from the PIC scheme. Hence, it suffices to show that the particle-to-grid transfer conserves the total linear momentum.

Furthermore, we note that it suffices to show that the extra terms in the APIC particle-to-grid transfer (Equation 22), comparing to the PIC transfer (Equation 15), sum to zero across both grids, i.e.

$$\frac{1}{2} \sum_{k \in \{\pm 1\}} \sum_i \sum_p w_{i,p,\mathcal{G}_k,t_n} m_p (\mathbf{B}_{p,t_n})_v^\alpha ((\mathbf{D}_{p,t_n})^{-1})_v^\beta (\mathbf{x}_{i,\mathcal{G}_k,t_n}^\beta - \mathbf{x}_{p,\mathcal{G}_0,t_n}^\beta) = 0$$

It is trivial to show that the above holds with property in Equation 8. \square

THEOREM B.2 (CONSERVATION OF ANGULAR MOMENTUM WITH APIC). *The total angular momentum is preserved in P2G, grid update, and P2G steps in APIC scheme by defining the total angular momentum of the grid as:*

$$\begin{aligned} \mathbf{L}_{\text{grid total},t_n}^\alpha &:= \frac{1}{2} \sum_{k \in \{\pm 1\}} \mathbf{L}_{\mathcal{G}_k,t_n}^\alpha \\ &= \frac{1}{2} \sum_{k \in \{\pm 1\}} \sum_i (\mathbf{x}_{i,\mathcal{G}_k,t_n} \times m_{i,\mathcal{G}_k,t_n} \mathbf{v}_{i,\mathcal{G}_k,t_n})^\alpha \end{aligned} \quad (32)$$

PROOF. In this part of the proof, we mainly follow the proof presented in the APIC paper. We first demonstrate that the P2G process will conserve angular momentum. Note that:

$$\begin{aligned} &\frac{1}{2} \sum_{k \in \{\pm 1\}} \sum_i \mathbf{x}_{i,\mathcal{G}_k,t_n}^\alpha \times m_{i,\mathcal{G}_k,t_n} \mathbf{v}_{i,\mathcal{G}_k,t_n}^\beta \\ &= \frac{1}{2} \sum_{k \in \{\pm 1\}} \sum_i \sum_p w_{i,p,\mathcal{G}_k,t_n} \mathbf{x}_{i,\mathcal{G}_k,t_n}^\alpha \times m_p \left(\mathbf{v}_{p,\mathcal{G}_0,t_n}^\beta \right. \\ &\quad \left. + (\mathbf{B}_{p,\mathcal{G}_0,t_n})_v^\beta ((\mathbf{D}_{p,\mathcal{G}_0,t_n})^{-1})_v^\mu (\mathbf{x}_{i,\mathcal{G}_k,t_n}^\mu - \mathbf{x}_{p,\mathcal{G}_0,t_n}^\mu) \right) \end{aligned}$$

We then simplify part of the equation as in APIC:

$$\begin{aligned} &\frac{1}{2} \sum_{k \in \{\pm 1\}} \sum_i \sum_p w_{i,p,\mathcal{G}_k,t_n} \mathbf{x}_{i,\mathcal{G}_k,t_n}^\alpha \times m_p (\mathbf{B}_{p,\mathcal{G}_0,t_n})_v^\beta \\ &\quad ((\mathbf{D}_{p,\mathcal{G}_0,t_n})^{-1})_v^\mu (\mathbf{x}_{i,\mathcal{G}_k,t_n}^\mu - \mathbf{x}_{p,\mathcal{G}_0,t_n}^\mu) \\ &= \frac{1}{2} \sum_{k \in \{\pm 1\}} \sum_i \sum_p m_p w_{i,p,\mathcal{G}_k,t_n} \delta^{\eta\gamma} \varepsilon_{\gamma\alpha\beta} \mathbf{x}_{i,\mathcal{G}_k,t_n}^\alpha (\mathbf{B}_{p,\mathcal{G}_0,t_n})_v^\beta \\ &\quad ((\mathbf{D}_{p,\mathcal{G}_0,t_n})^{-1})_v^\mu (\mathbf{x}_{i,\mathcal{G}_k,t_n}^\mu - \mathbf{x}_{p,\mathcal{G}_0,t_n}^\mu) \\ &= \frac{1}{2} \sum_p m_p \delta^{\eta\gamma} \varepsilon_{\gamma\alpha\beta} (\mathbf{B}_{p,\mathcal{G}_0,t_n})_v^\beta ((\mathbf{D}_{p,\mathcal{G}_0,t_n})^{-1})_v^\mu \sum_{k \in \{\pm 1\}} \sum_i \\ &\quad w_{i,p,\mathcal{G}_k,t_n} \left((\mathbf{x}_{i,\mathcal{G}_k,t_n}^\alpha - \mathbf{x}_{p,\mathcal{G}_0,t_n}^\alpha) (\mathbf{x}_{i,\mathcal{G}_k,t_n}^\mu - \mathbf{x}_{p,\mathcal{G}_0,t_n}^\mu) \right. \\ &\quad \left. + \mathbf{x}_{p,\mathcal{G}_0,t_n}^\alpha (\mathbf{x}_{i,\mathcal{G}_k,t_n}^\mu - \mathbf{x}_{p,\mathcal{G}_0,t_n}^\mu) \right) \\ &= \frac{1}{2} \sum_p m_p \delta^{\eta\gamma} \varepsilon_{\gamma\alpha\beta} (\mathbf{B}_{p,\mathcal{G}_0,t_n})_v^\beta ((\mathbf{D}_{p,\mathcal{G}_0,t_n})^{-1})_v^\mu \sum_{k \in \{\pm 1\}} \sum_i \\ &\quad w_{i,p,\mathcal{G}_k,t_n} \left((\mathbf{x}_{i,\mathcal{G}_k,t_n}^\alpha - \mathbf{x}_{p,\mathcal{G}_0,t_n}^\alpha) (\mathbf{x}_{i,\mathcal{G}_k,t_n}^\mu - \mathbf{x}_{p,\mathcal{G}_0,t_n}^\mu) \right) \\ &= \sum_p m_p \delta^{\eta\gamma} \varepsilon_{\gamma\alpha\beta} (\mathbf{B}_{p,\mathcal{G}_0,t_n})_v^\beta ((\mathbf{D}_{p,\mathcal{G}_0,t_n})^{-1})_v^\mu \left(\right. \\ &\quad \left. \frac{1}{2} \sum_{k \in \{\pm 1\}} \sum_i w_{i,p,\mathcal{G}_k,t_n} ((\mathbf{x}_{i,\mathcal{G}_k,t_n})^\alpha - (\mathbf{x}_{p,\mathcal{G}_0,t_n})^\alpha) \right. \\ &\quad \left. (\mathbf{x}_{i,\mathcal{G}_k,t_n}^\mu - \mathbf{x}_{p,\mathcal{G}_0,t_n}^\mu) \right) \\ &= \sum_p m_p \delta^{\eta\gamma} \varepsilon_{\gamma\alpha\beta} (\mathbf{B}_{p,\mathcal{G}_0,t_n})_v^\beta ((\mathbf{D}_{p,\mathcal{G}_0,t_n})^{-1})_v^\mu (\mathbf{D}_{p,\mathcal{G}_0,t_n})_v^\mu \\ &= \sum_p m_p \delta^{\eta\gamma} \varepsilon_{\gamma\alpha\beta} (\mathbf{B}_{p,\mathcal{G}_0,t_n})_v^\beta \end{aligned}$$

Hence, we note that the total angular momentum can be reduced to:

$$\begin{aligned} &\frac{1}{2} \sum_{k \in \{\pm 1\}} \sum_i \sum_p (w_{i,p,\mathcal{G}_k,t_n} \mathbf{x}_{i,\mathcal{G}_k,t_n} \times m_p \mathbf{v}_{p,\mathcal{G}_0,t_n})^\eta \\ &\quad + \sum_p m_p \delta^{\eta\gamma} \varepsilon_{\gamma\alpha\beta} (\mathbf{B}_{p,\mathcal{G}_0,t_n})_v^\beta \alpha \\ &= \sum_p (\mathbf{x}_{p,\mathcal{G}_0,t_n} \times m_p \mathbf{v}_{p,\mathcal{G}_0,t_n})^\eta + \sum_p m_p \delta^{\eta\gamma} \varepsilon_{\gamma\alpha\beta} (\mathbf{B}_{p,\mathcal{G}_0,t_n})_v^\beta \alpha \end{aligned} \quad (33)$$

Following APIC formulation, we also define Equation 33 to be the total angular momentum on particles. This concludes the proof for the conservation of angular momentum in the particle-to-grid step.

For the grid evolution step, we first note that $\mathbf{F}_{p,\mathcal{G}_0,t_n}$ and $\mathbf{P}_{p,\mathcal{G}_0,t_n}$ shares the same singular space for isotropic materials, i.e. if the singular value decomposition is in form of

$$\mathbf{F}_{p,\mathcal{G}_0,t_n} = \mathbf{U}_{p,\mathcal{G}_0,t_n} \Sigma_{p,\mathcal{G}_0,t_n} \mathbf{V}_{p,\mathcal{G}_0,t_n} \quad (34)$$

then we would have $\mathbf{P}_{p, \mathcal{G}_0, t_n} = \mathbf{U}_{p, \mathcal{G}_0, t_n} \hat{\Sigma}_{p, \mathcal{G}_0, t_n} \mathbf{V}_{p, \mathcal{G}_0, t_n}$. This implies that:

$$(\mathbf{P}_{p, \mathcal{G}_0, t_n})^\alpha_\beta = (\mathbf{F}_{p, \mathcal{G}_0, t_n})^\alpha_\nu (\mathbf{A}_{p, \mathcal{G}_0, t_n})^\nu_\mu \quad (35)$$

where $(\mathbf{A}_{p, \mathcal{G}_0, t_n})^\alpha_\beta = ((\mathbf{V}_{p, \mathcal{G}_0, t_n})^T)^\alpha_\nu (\hat{\Sigma}_{p, \mathcal{G}_0, t_n})^\nu_\mu (\mathbf{V}_{p, \mathcal{G}_0, t_n})^\mu_\beta$ is a symmetric matrix.

Then, we denote

$$(\mathbf{G}_{p, \mathcal{G}_0, t_n})^\alpha_\beta = \frac{1}{2} \sum_{k \in \{\pm 1\}} \sum_i \tilde{\mathbf{x}}_{i, \mathcal{G}_k, t^{n+1}}^\alpha ((\nabla w_{i, p, k, t_n})^T)_\beta \quad (36)$$

We see that:

$$\begin{aligned} & (\mathbf{F}_{p, \mathcal{G}_0, t^{n+1}})^\alpha_\beta \\ &= (\delta^\alpha_\nu + \frac{\Delta t}{2} \sum_{k \in \{\pm 1\}} \sum_i \tilde{\mathbf{v}}_{i, \mathcal{G}_k, t^{n+1}}^\alpha ((\nabla w_{i, p, \mathcal{G}_k, t_n})^T)_\nu) (\mathbf{F}_{p, \mathcal{G}_0, t_n})^\nu_\beta \\ &= (\delta^\alpha_\nu + \frac{1}{2} \sum_{k \in \{\pm 1\}} \sum_i (\tilde{\mathbf{x}}_{i, \mathcal{G}_k, t^{n+1}}^\alpha - \mathbf{x}_{i, \mathcal{G}_k, t_n}^\alpha) ((\nabla w_{i, p, \mathcal{G}_k, t_n})^T)_\nu) \\ & \quad (\mathbf{F}_{p, \mathcal{G}_0, t_n})^\nu_\beta \\ &= (\delta^\alpha_\nu + (\mathbf{G}_{p, \mathcal{G}_0, t^{n+1}})^\alpha_\nu - \delta^\alpha_\nu) (\mathbf{F}_{p, \mathcal{G}_0, t_n})^\nu_\beta \\ &= (\mathbf{G}_{p, \mathcal{G}_0, t^{n+1}})^\alpha_\nu (\mathbf{F}_{p, \mathcal{G}_0, t_n})^\nu_\beta \end{aligned}$$

Hence, with Equation 35, we observe that:

$$\begin{aligned} & \frac{1}{2} \sum_{k \in \{\pm 1\}} \sum_i (\mathbf{x}_{i, \mathcal{G}_k, t_n} \times \mathbf{f}_{i, \mathcal{G}_k, t_n})^\alpha \\ &= \frac{1}{2} \sum_{k \in \{\pm 1\}} \sum_i \delta^{\alpha\beta} \epsilon_{\beta\gamma\mu} \mathbf{x}_{i, \mathcal{G}_k, t_n}^\gamma \mathbf{f}_{i, \mathcal{G}_k, t_n}^\mu \\ &= \frac{1}{2} \sum_{k \in \{\pm 1\}} \sum_i \delta^{\alpha\beta} \epsilon_{\beta\gamma\mu} \mathbf{x}_{i, \mathcal{G}_k, t_n}^\gamma \left(\sum_p V_0 (\mathbf{P}_{p, \mathcal{G}_0, t_n})^\mu_\eta ((\mathbf{F}_{p, \mathcal{G}_0, t_n})^T)_\nu^\eta (\nabla w_{i, p, \mathcal{G}_k, t_n})^\nu \right) \\ &= V_0 \sum_p \delta^{\alpha\beta} \epsilon_{\beta\gamma\mu} (\mathbf{P}_{p, \mathcal{G}_0, t_n})^\mu_\eta ((\mathbf{F}_{p, \mathcal{G}_0, t_n})^T)_\nu^\eta \delta^{\nu\xi} \left(\frac{1}{2} \sum_{k \in \{\pm 1\}} \sum_i \mathbf{x}_{i, \mathcal{G}_k, t_n}^\gamma ((\nabla w_{i, p, \mathcal{G}_k, t_n})^T)_\xi \right) \\ &= V_0 \sum_p \delta^{\alpha\beta} \epsilon_{\beta\gamma\mu} (\mathbf{P}_{p, \mathcal{G}_0, t_n})^\mu_\eta ((\mathbf{F}_{p, \mathcal{G}_0, t_n})^T)_\nu^\eta \delta^{\nu\gamma} \\ &= V_0 \sum_p \delta^{\alpha\beta} \epsilon_{\beta\gamma\mu} (\mathbf{F}_{p, \mathcal{G}_0, t_n})^\mu_\xi (\mathbf{A}_{p, \mathcal{G}_0, t_n})^\xi_\eta ((\mathbf{F}_{p, \mathcal{G}_0, t_n})^T)_\gamma^\eta \\ &= 0 \end{aligned}$$

where the last equation holds since \mathbf{FAF}^T (with subscripts p, \mathcal{G}_0, t_n) is symmetric. From above, it is then true that:

$$\frac{1}{2} \sum_{k \in \{\pm 1\}} \sum_i (\mathbf{x}_{i, \mathcal{G}_k, t_n} \times m_{i, \mathcal{G}_k, t_n} (\tilde{\mathbf{v}}_{i, \mathcal{G}_k, t^{n+1}} - \mathbf{v}_{i, \mathcal{G}_k, t_n})) = 0$$

Therefore, we may conclude with:

$$\begin{aligned} & \frac{1}{2} \sum_{k \in \{\pm 1\}} \sum_i \left((\tilde{\mathbf{x}}_{i, \mathcal{G}_k, t^{n+1}} \times m_{i, \mathcal{G}_k, t_n} \tilde{\mathbf{v}}_{i, \mathcal{G}_k, t^{n+1}})^\alpha \right. \\ & \quad \left. - (\mathbf{x}_{i, \mathcal{G}_k, t_n} \times m_{i, \mathcal{G}_k, t_n} \mathbf{v}_{i, \mathcal{G}_k, t_n})^\alpha \right) \\ &= \frac{1}{2} \sum_{k \in \{\pm 1\}} \sum_i \left((\tilde{\mathbf{x}}_{i, \mathcal{G}_k, t^{n+1}} \times m_{i, \mathcal{G}_k, t_n} \tilde{\mathbf{v}}_{i, \mathcal{G}_k, t^{n+1}})^\alpha \right. \\ & \quad \left. - (\mathbf{x}_{i, \mathcal{G}_k, t_n} \times m_{i, \mathcal{G}_k, t_n} \mathbf{v}_{i, \mathcal{G}_k, t_n})^\alpha \right) \\ & \quad - \frac{1}{2} \sum_{k \in \{\pm 1\}} \sum_i (\mathbf{x}_{i, \mathcal{G}_k, t_n} \times m_{i, \mathcal{G}_k, t_n} (\tilde{\mathbf{v}}_{i, \mathcal{G}_k, t^{n+1}} - \mathbf{v}_{i, \mathcal{G}_k, t_n}))^\alpha \\ &= \frac{1}{2} \sum_{k \in \{\pm 1\}} \sum_i ((\tilde{\mathbf{x}}_{i, \mathcal{G}_k, t^{n+1}} - \mathbf{x}_{i, \mathcal{G}_k, t_n}) \times m_{i, \mathcal{G}_k, t_n} \tilde{\mathbf{v}}_{i, \mathcal{G}_k, t^{n+1}})^\alpha \\ &= \frac{\Delta t}{2} \sum_{k \in \{\pm 1\}} \sum_i (\tilde{\mathbf{v}}_{i, \mathcal{G}_k, t^{n+1}} \times m_{i, \mathcal{G}_k, t_n} \tilde{\mathbf{v}}_{i, \mathcal{G}_k, t^{n+1}}) \\ &= 0 \end{aligned}$$

Hence, we see that the grid update step also conserves angular momentum.

Finally, for the grid-to-particle transfer step, we note that:

$$\begin{aligned} & \sum_p (\mathbf{x}_{p, \mathcal{G}_0, t^{n+1}} \times m_p \mathbf{v}_{p, \mathcal{G}_0, t^{n+1}})^\alpha + \sum_p m_p \delta^{\alpha\beta} \epsilon_{\beta\gamma\mu} (\mathbf{B}_{p, \mathcal{G}_0, t^{n+1}})^\mu_\nu \\ &= \sum_p (\mathbf{x}_{p, \mathcal{G}_0, t^{n+1}} \times m_p \mathbf{v}_{p, \mathcal{G}_0, t^{n+1}})^\alpha + \frac{1}{2} \sum_p \sum_{k \in \{\pm 1\}} \sum_i m_p \delta^{\alpha\beta} \epsilon_{\beta\gamma\mu} \\ & \quad w_{i, p, \mathcal{G}_k, t_n} \tilde{\mathbf{v}}_{i, \mathcal{G}_k, t^{n+1}}^\mu ((\mathbf{x}_{i, \mathcal{G}_k, t_n} - \mathbf{x}_{p, \mathcal{G}_0, t_n})^T)_\nu \\ &= \frac{1}{2} \sum_p m_p \sum_{k \in \{\pm 1\}} \sum_i \left(w_{i, p, \mathcal{G}_k, t_n} \delta^{\alpha\eta} \epsilon_{\eta\gamma\xi} \mathbf{x}_{p, \mathcal{G}_0, t^{n+1}}^\gamma \tilde{\mathbf{v}}_{i, \mathcal{G}_k, t^{n+1}}^\xi \right. \\ & \quad \left. + w_{i, p, \mathcal{G}_k, t_n} \delta^{\alpha\beta} \epsilon_{\beta\gamma\mu} \tilde{\mathbf{v}}_{i, \mathcal{G}_k, t^{n+1}}^\mu ((\mathbf{x}_{i, \mathcal{G}_k, t_n} - \mathbf{x}_{p, \mathcal{G}_0, t_n})^T)_\nu \right) \\ &= \frac{1}{2} \sum_p m_p \sum_{k \in \{\pm 1\}} \sum_i \left(w_{i, p, \mathcal{G}_k, t_n} \delta^{\alpha\eta} \epsilon_{\eta\gamma\xi} \tilde{\mathbf{v}}_{i, \mathcal{G}_k, t^{n+1}}^\xi \right. \\ & \quad \left. (\mathbf{x}_{p, \mathcal{G}_0, t^{n+1}}^\gamma + (\mathbf{x}_{i, \mathcal{G}_k, t_n} - \mathbf{x}_{p, \mathcal{G}_0, t_n})^\gamma) \right) \\ &= \sum_p \delta^{\alpha\eta} \epsilon_{\eta\gamma\xi} \Delta t v_{p, \mathcal{G}_0, t^{n+1}}^\gamma m_p \left(\frac{1}{2} \sum_{k \in \{\pm 1\}} \sum_i w_{i, p, \mathcal{G}_k, t_n} \tilde{\mathbf{v}}_{i, \mathcal{G}_k, t^{n+1}}^\xi \right) \\ & \quad + \frac{1}{2} \sum_{k \in \{\pm 1\}} \sum_i \delta^{\alpha\beta} \epsilon_{\beta\gamma\mu} \mathbf{x}_{i, \mathcal{G}_k, t_n}^\gamma \tilde{\mathbf{v}}_{i, \mathcal{G}_k, t^{n+1}}^\mu \sum_p m_p w_{i, p, \mathcal{G}_k, t_n} \\ &= \frac{1}{2} \sum_{k \in \{\pm 1\}} \sum_i \left(m_{i, \mathcal{G}_k, t_n} \delta^{\alpha\eta} \epsilon_{\eta\gamma\mu} \mathbf{x}_{i, \mathcal{G}_k, t_n}^\gamma \tilde{\mathbf{v}}_{i, \mathcal{G}_k, t^{n+1}}^\mu \right) \\ &= \frac{1}{2} \sum_{k \in \{\pm 1\}} \sum_i \mathbf{x}_{i, \mathcal{G}_k, t_n} \times m_{i, \mathcal{G}_k, t_n} \tilde{\mathbf{v}}_{i, \mathcal{G}_k, t^{n+1}} \end{aligned}$$

Therefore, it concludes the proof for the conservation of angular momentum in the G2P step. \square